A Godunov-Type Finite Volume Method for Systems of Shallow Water Equations

S. Chippada
C. Dawson
M. Martinez
M. Wheeler

CRPC-TR97687
January 1997

Center for Research on Parallel Computation
Rice University
6100 South Main Street
CRPC - MS 41
Houston, TX 77005

submitted 2/97

A Godunov-type Finite Volume Method for the System of Shallow Water Equations

S. Chippada, C. N. Dawson, M. L. Martinez, and M. F. Wheeler

January 23, 1997

Abstract

A finite volume based numerical algorithm has been developed for the numerical solution of the system of shallow water equations. The algorithm is a Godunov type method and solves the Riemann problem approximately using Roe's technique. The algorithm is developed in 2-D with arbitrary triangulations and conserves all primary variables such as mass and momentum. The procedure is implemented on some simple test cases and some complex coastal flow problems. The algorithm is shown to produce excellent results without spurious oscillations and agrees very well with known analytical results and predictions made by wave equation formulations of the shallow water equations. The basic Godunov method is also extended to second-order accuracy through a slope-limiter type algorithm.

1 INTRODUCTION

The Shallow Water Equations (SWE) are used to describe free surface hydrodynamics in vertically well-mixed water bodies where the horizontal length scales are much greater than the fluid depth (i.e., long wavelength phenomena). The SWE are obtained by assuming hydrostatic pressure distribution, and by integrating the three-dimensional incompressible Navier-Stokes equations along the depth of the fluid body. Most of the naturally occurring fluid flows are turbulent, and a uniform velocity profile is assumed in the vertical direction. With these assumptions, the three-dimensional free boundary problem reduces to a two-dimensional fixed boundary problem with the primary variables being the vertical averages of the horizontal fluid velocities and the fluid depth (see Weiyan (1992) for a derivation of the shallow water equations). The SWE can be used to study many physical phenomena of interest, such as storm surges, tidal fluctuations, tsunami waves, forces acting on off-shore structures, and contaminant and salinity transport (Kinnmark, 1985).

Numerical solution of the SWE is made challenging due to many factors. The SWE are a system of coupled nonlinear conservation laws which need to be solved on complicated physical domains arising from irregular coast-lines and islands. The bottom sea bed (bathymetry) is often very irregular. Shallow water systems are subjected to a wide variety of phenomena such as the Coriolis force, the surface wind stress, atmospheric pressure gradient, and tidal potential forces. In addition to these physical factors there are

additional difficulties arising from the mathematical nature of the SWE. Most important is the coupling between the fluid depth and the horizontal velocity field which could lead to spurious spatial oscillations if the numerical algorithms are not chosen with care.

Several numerical algorithms have been developed over the years for the SWE. These numerical algorithms can be classified into two broad categories. In the first category, the primitive form of the SWE that are obtained from the direct vertical integration of the 3D incompressible Navier-Stokes, are numerically solved. However, a straight forward use of equal-order interpolation spaces in the finite element context or the use of non-staggered grids in the finite difference context can lead to spurious spatial oscillations due to the nonlinear coupling between the fluid depth and the horizontal velocity field. These spatial oscillations can be minimized and/or eliminated through the use of staggered grids or mixed interpolation spaces. For example, King and Norton (1978) approximate velocities through piecewise quadratic and elevations using piecewise linear basis functions. Several numerical methods based on the primitive SWE and equal order approximations have also been developed (e.g., Kawahara et al. (1982), Szymkiewicz (1993), Zienkiewicz and Ortiz (1995)). If the spurious spatial oscillations are suppressed through careful splitting between the elevation and velocity field, the numerical procedures based on staggered or equal order approximations are generally considered to be more efficient from an implementation point of view. In the second category, the primitive SWE are reformulated and the first-order hyperbolic form of the primitive continuity equation is replaced with a second-order wave equation (Lynch and Gray (1979), Luettich et al. (1991)). Clearly, the elevation-velocity coupling has played an important role in the development of numerical algorithms for shallow water systems.

In this paper we take a slightly different view of the SWE. The SWE are a system of conservation laws. Mathematically the SWE are very similar to the compressible Euler and Navier-Stokes equations with the compressibility coming from the finite speed of the surface gravity wave. A rich variety of numerical methods have been developed for compressible Euler equations, and these are extended to the SWE in this paper. In particular, we consider the Godunov-type finite volume method which has been shown to be a stable, monotonic procedure (Godunov 1959, Hirsch 1990, LeVeque 1992). This numerical procedure conserves mass and momentum locally, and can model discontinuities such as shocks. Alcrudo and Garcia-Navarro (1993) used a Godunov-type finite volume method for the SWE. The present paper applies the procedure to unstructured meshes based on linear triangles. The efficiency and accuracy for realistic coastal flow problems is established and comparisons are made with the generalized wave continuity equation formulation of Luettich *et al.* (1991).

In §2 the mathematical model including the boundary conditions is described. The basic Godunov-type finite volume method is described in §3. In §4, supercritical channel flows encountering sudden change

in cross-section and complex coastal flow problems are studied and their accuracy established through comparison to analytical results and numerical results based on the wave formulation of Luettich *at al* (1991). The basic numerical method is extended to higher-order spatial accuracy in §5 through a slope-limiting procedure. Finally, in §6 we conclude with some remarks on future work.

2 MATHEMATICAL MODEL

Vertical integration of the 3-D incompressible Navier–Stokes equations along with the assumptions of a hydrostatic pressure and a vertically uniform horizontal velocity profile results in the Shallow Water Equations (SWE) of the following form:

$$\frac{\partial \xi}{\partial t} + \nabla \cdot (\mathbf{u}H) = 0, \tag{1}$$

$$\frac{\partial \mathbf{u}}{\partial t} + \mathbf{u} \cdot \nabla \mathbf{u} + \tau_{bf}\mathbf{u} + f_c \mathbf{k} \times \mathbf{u} + g\nabla\xi - \frac{1}{H}\nabla \cdot \left[\nu_T H \left(\nabla \mathbf{u} + \nabla \mathbf{u}^T\right)\right] = \frac{1}{H}\mathbf{F}. \tag{2}$$

Eq.1 represents the conservation of mass and is also referred to as the primitive continuity equation (PCE). Eq.2 represents the conservation of momentum in non-conservative form (NCME). In the above equations, ξ represents the deflection of the air-liquid interface from the mean sea level, $H = h_b + \xi$ represents the total fluid depth, and h_b is the bathymetric depth (see Fig.1), $\mathbf{u}$ = (u,v) is the depth averaged horizontal velocity field, f_c is the Coriolis parameter resulting from the earth's rotation, $\mathbf{k}$ is the local vertical vector, g is the gravitational acceleration, τ_{bf} is the bottom friction coefficient which is usually computed using either the Manning's or the Chezy's friction law, and ν_T is the depth averaged turbulent viscosity. In addition to the above described phenomena, often we need to include the effects of surface wind stress, variable atmospheric pressure and tidal potentials which are expressed through the body force $\mathbf{F}$ (Luettich *et al.*, 1991). The eddy viscosity coefficient ν_T is usually computed using a turbulence closure model. However, in most situations the bottom friction dominates lateral diffusion and dispersion, and the parameter ν_T is set to zero in the subsequent discussion. The conservative form of the momentum equation (CME) can be derived by combining Eqs.1 and 2, resulting in:

$$\frac{\partial \mathbf{u}H}{\partial t} + \nabla \cdot (\mathbf{u}\mathbf{u}H) + \tau_{bf}\mathbf{u}H + f_c \mathbf{k} \times \mathbf{u}H + gH\nabla\xi = \mathbf{F} \tag{3}$$

Thus, the continuity equation (Eq.1) along with the nonconservative momentum equation (Eq.2) or the conservative momentum equation (Eq.3) represent the shallow water equations system in the primitive form (P-SWE) and are solved, usually numerically, for ξ and $\mathbf{u}$.

Numerical models based on the P-SWE have been found to be susceptible to spurious spatial oscillations. These oscillations are a result of the finite spatial discretization and exhibit themselves as internode ('$2\Delta x$') oscillations (Walters and Carey 1981). Several numerical procedures have been developed to overcome this

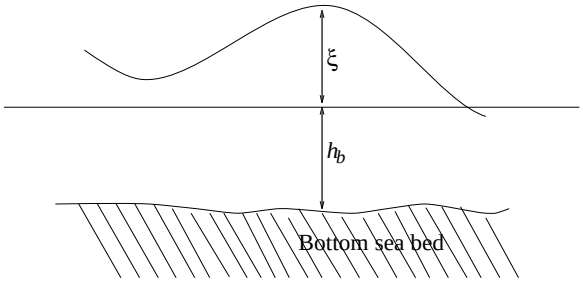

Figure 1: Definition of elevation and bathymetry

problem including mixed interpolation spaces and the wave equation formulations. In this paper we make direct comparisons with the Generalized Wave Continuity Equation (GWCE) formulation of Lynch and Gray (1979), which has been refined over the years to the form described in Luettich *et al.* (1991). In this formulation, the PCE is replaced with a second-order wave equation, called the GWCE which is derived as follows:

$$GWCE \equiv \frac{\partial}{\partial t}\left(PCE\right) - \nabla \cdot \left(CME\right) + \tau_0 \left(PCE\right) = 0. \tag{4}$$

The GWCE in its final form is given by:

$$\frac{\partial^2 \xi}{\partial t^2} + \tau_0 \frac{\partial \xi}{\partial t} - \nabla \cdot \left(gH\nabla\xi\right) - \nabla \cdot \left[\left(\tau - \tau_0\right)\nabla \cdot \left(\mathbf{u}H\right) + \nabla \cdot \left(\mathbf{u}\mathbf{u}H\right) + f_c \mathbf{k} \times \mathbf{u}H\right] = 0. \tag{5}$$

The GWCE formulation as described in Luettich *et al.* (1991) solves the GWCE (Eq.5) along with the NCME (Eq.2) for ξ and $\mathbf{u}$. Note that, PCE, a first-order hyperbolic equation, is replaced with the GWCE, a second-order wave equation. Even with equal-order interpolation spaces for ξ and $\mathbf{u}$, the GWCE formulation is shown to produce stable results without any spatial oscillations. The absence of spurious spatial oscillations in the GWCE formulation is attributed to the monotonic dispersion relation between the wave speed and the wave length of the disturbance.

The boundary conditions for the shallow water equations could be any one of following:

1. *Land boundary:* The boundary condition on the land is of the no-flow type written as:

$$\mathbf{u} \cdot \nu = 0, \quad \text{and} \quad \frac{\partial \xi}{\partial n} = 0. \tag{6}$$

2. *River boundary:* River boundaries bring in discharge into the system and the boundary conditions are written as:

$$\mathbf{u} \cdot \nu = \hat{\mathbf{u}} \cdot \nu, \qquad and \quad \xi = \hat{\xi}. \tag{7}$$

3. *Open sea boundary:* The open sea boundary conditions are written as:

$$\xi = \hat{\xi}(t), \quad \text{and} \quad \frac{\partial \mathbf{u}}{\partial n} = 0. \tag{8}$$

In addition, in numerical computations we often shorten the domain artificially, and in such instances we would want to impose radiation-type boundary conditions.

The initial conditions are given by:

$$\xi = \xi_0 \ ; \ \mathbf{u} = \mathbf{u}_0 \tag{9}$$

The initial conditions need to satisfy the following compatibility condition:

$$\frac{\partial \xi_0}{\partial t} + \nabla \cdot (\mathbf{u}_0 H_0) = 0. \tag{10}$$

In geophysical flow simulations, the initial conditions are often impossible to measure, and in such instances a cold start simulation is performed. In cold start simulations, the fluid domain is assumed to be at rest initially ($\xi = 0$, $\mathbf{u} = 0$) and the boundary conditions and forcing functions are applied gradually through a ramp function.

3 NUMERICAL MODELING

Our numerical algorithm is based on the solution of the primitive SWE, namely, the PCE (Eq.1) and the CME (Eq.3), and uses a Godunov-type finite volume method. The system of SWE given by the PCE and the CME are rewritten in the following compact vector form:

$$\frac{\partial \mathbf{c}}{\partial t} + \frac{\partial \mathbf{f}}{\partial x} + \frac{\partial \mathbf{g}}{\partial y} = \mathbf{h} \tag{11}$$

where,

$$\mathbf{c} = \begin{pmatrix} \xi \\ U \\ V \end{pmatrix}; \quad \mathbf{f} = \begin{pmatrix} U \\ \frac{U^2}{H} - \frac{1}{2} g \left(H^2 - h_b^2 \right) \\ \frac{UV}{H} \end{pmatrix}; \quad \mathbf{g} = \begin{pmatrix} V \\ \frac{UV}{H} \\ \frac{V^2}{H} - \frac{1}{2} g \left(H^2 - h_b^2 \right) \end{pmatrix}; \tag{12}$$

and,

$$\mathbf{h} = \begin{pmatrix} 0 \\ -\tau_{bf} U + f_c V + g \xi \frac{\partial h_b}{\partial x} + F_x \\ -\tau_{bf} V - f_c U + g \xi \frac{\partial h_b}{\partial y} + F_y \end{pmatrix}. \tag{13}$$

The primary variables are ξ and $\mathbf{U} = \mathbf{u}H$, and $g\left(H^2 - h_b^2\right)/2$ can be interpreted as the fluid pressure. (F_x, F_y) are the additional body forces arising from wind stress, atmospheric pressure gradient, tide potential, etc. Note that, even if none of these afore mentioned body forces are present, we would still be left with non-homogeneous momentum equations as long as the bathymetry varies spatially, i.e., $(\nabla h_b \neq 0)$.

The primary variables (ξ, U, V) are discretized as piece-wise constants within the area enclosed by the linear triangles, as shown in Fig.2. These element averages are updated each time step through the fluxes crossing the element edges and the body forces acting on the volume of the element. Thus, we discretize the integral formulation of the system of shallow water equations, rather than the differential form, numerically.

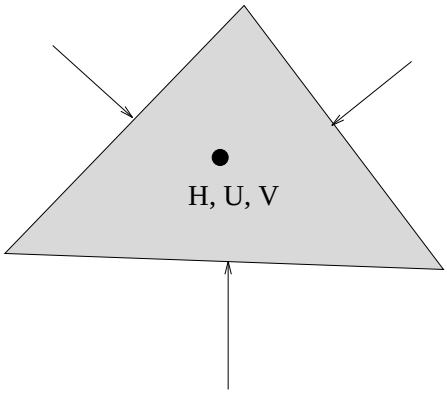

Figure 2: Typical control volume

The integral formulation for the hyperbolic system (Eq.11) is given by:

$$\frac{\partial}{\partial t}\int_{\Omega_e} \mathbf{c}\, d\Omega_e + \int_{\Gamma_e} \mathbf{f_n}\, d\Gamma_e = \int_{\Omega_e} \mathbf{h}\, d\Omega_e \tag{14}$$

where, $\mathbf{f_n} = \mathbf{f}n_x + \mathbf{g}n_y$ is the normal flux crossing the boundary of the control volume. In the above equations, Ω_e and Γ_e are, respectively, the area and the boundary of the element, $\mathbf{n} = (n_x, n_y)$ is the outward pointing unit normal vector of the boundary Γ_e.

For triangular control volumes such as that shown in Fig.2, the time discretized equations would be:

$$\frac{{\mathbf{c}_e}^{n+1} - {\mathbf{c}_e}^{n}}{\Delta t}\Omega_e + \sum_{i=1}^{i=3} \left(\mathbf{f}^n_{n_i}\Gamma_i\right) = \mathbf{h}^n\Omega_e. \tag{15}$$

The superscript represents the time level, and the element averages of the primary variables are updated explicitly each time step, once the normal fluxes at the element edges are known. Note that the primary variables ξ, U and V are discretized as constant values with in the cell, and are discontinuous across the element edges. The normal flux at the edge can easily be computed through one of the following averages:

$$\mathbf{f}_n = \frac{1}{2}\left(\mathbf{f}_n\left(\mathbf{c}_L\right) + \mathbf{f}_n\left(\mathbf{c}_R\right)\right) \quad ; \quad \text{(or)} \quad ; \quad \mathbf{f}_n = \mathbf{f}_n\left(\frac{\mathbf{c}_L + \mathbf{c}_R}{2}\right) \tag{16}$$

However, a simple averaging, such as that shown above, would result in a centered spatial approximation, and the resulting numerical algorithm would be unstable. The shallow water equations without the viscous terms are nothing but a set of first-order hyperbolic conservation laws, and are very similar to the compressible Euler equations arising in gas dynamics. A rich variety of methods have been constructed for the compressible Euler equations, and some of the ideas developed in this context are extended to the shallow water equations.

The Godunov method is one of the most successful approaches that has been developed for solving first-order hyperbolic system of equations (Godunov 1959, Hirsch 1990, LeVeque 1992). In this approach, the variables are approximated as averages within the element volumes, and the advective flux at the cell

interface is computed by solving the Riemann shock-tube problem. Thus, the fluxes computed at the element edges are the exact analytical fluxes we would have had if there were two constant states to either side of the edge. The discontinuities propagate with the right velocities and without any spurious oscillations. All variables are locally conserved and the classical Godunov approach gives us a stable, monotonic numerical algorithm (LeVeque 1992).

The quasi-linear form of the hyperbolic system (Eq.11) is given by:

$$\frac{\partial \mathbf{c}}{\partial t} + \mathbf{A}\frac{\partial \mathbf{c}}{\partial x} + \mathbf{B}\frac{\partial \mathbf{c}}{\partial y} = \mathbf{h} \tag{17}$$

where $\mathbf{A} = \frac{\partial \mathbf{f}}{\partial \mathbf{c}}$, and $\mathbf{B} = \frac{\partial \mathbf{g}}{\partial \mathbf{c}}$. This is a nonlinear problem with $\mathbf{A}$ and $\mathbf{B}$ being functions of $\mathbf{c}$. The local 1-D Riemann problem is posed by considering the interaction of the two discontinuous states in the direction normal to the cell interface. Note that, the quantity of interest in the integral formulation (Eq.14) is the normal flux ($\mathbf{f}_n$) crossing the cell interface. The normal Jacobian matrix $\mathbf{A}_n$ is found to be:

$$\mathbf{A}_n = \begin{bmatrix} 0 & n_x & n_y \\ n_x\left(a^2 - u^2\right) - n_y uv & 2n_x u + n_y v & n_y u \\ n_y\left(a^2 - v^2\right) - n_x uv & n_x v & 2n_y v + n_x u \end{bmatrix} \tag{18}$$

where, $a^2 = gH$. The eigenvalues and the corresponding eigenvectors for the normal Jacobian ($\mathbf{A}_n$) are given by:

$$\lambda_1 = u_n - \sqrt{gH} \;\; ; \;\; \mathbf{r}_1 = \begin{Bmatrix} 1 \\ u - \sqrt{gH}n_x \\ v - \sqrt{gH}n_y \end{Bmatrix} \tag{19}$$

$$\lambda_2 = u_n \;\; ; \;\; \mathbf{r}_2 = \begin{Bmatrix} 0 \\ -n_y \\ n_x \end{Bmatrix} \tag{20}$$

$$\lambda_3 = u_n + \sqrt{gH} \;\; ; \;\; \mathbf{r}_3 = \begin{Bmatrix} 1 \\ u + \sqrt{gH}n_x \\ v + \sqrt{gH}n_y \end{Bmatrix} \tag{21}$$

In the case of a pure 1-D problem, we would have only the eigenvalues: $(u_n - \sqrt{gH},\, u_n + \sqrt{gH})$. An additional eigenvalue equal to u_n arises in the case of 2-D. Eigenvalues λ_1 and λ_3 result in either a compression wave (shock) or a rarefaction wave depending on the left and right states. All primary variables are discontinuous across the shock and continuous across rarefaction waves. The eigenvalue λ_2 is linearly degenerate and gives rise to a contact discontinuity, where, only the tangential velocity is discontinuous and the normal velocity and fluid depth are continuous. Eventhough the cell interface Riemann problem can be solved in an exact manner, they often require the solution of a set of nonlinear algebraic equations, which can be very time consuming. Moreover, the higher order accuracy obtained through the exact calculation of the fluxes is lost due to the cell averaging done at the end of the flux calculation, since the primary variables are only represented as averages within cell volumes. Thus, a number of approximate Riemann solvers have been

constructed to solve the Riemann problem in an efficient manner and Roe's approximation is one of them. In this paper the 1-D Riemann problem at the cell interface is solved using Roe's approximation.

In Roe's approximation, the nonlinear problem is linearized at the cell interface (Roe 1981, LeVeque 1992). At the cell interface we have a discontinuity with state $\mathbf{c}_L$ on the left side and state $\mathbf{c}_R$ on the right side. In Roe's approximation, Eq.17 is linearized as follows:

$$\frac{\partial \mathbf{c}}{\partial t} + \hat{\mathbf{A}}\left(\mathbf{c}_L, \mathbf{c}_R\right) \frac{\partial \mathbf{c}}{\partial x} + \hat{\mathbf{B}}\left(\mathbf{c}_L, \mathbf{c}_R\right) \frac{\partial \mathbf{c}}{\partial y} = \mathbf{h} \tag{22}$$

where, $\hat{\mathbf{A}}$ and $\hat{\mathbf{B}}$ are linearized forms of $\mathbf{A}$ and $\mathbf{B}$, respectively. Eventhough there is more than one way to compute the linearized matrices $\hat{\mathbf{A}}$ and $\hat{\mathbf{B}}$, it is desired that the linearized matrices satisfy certain properties. Important among them is that the Rankine-Hugoniot jump conditions be satisfied across the disconituity, i.e.,

$$[\mathbf{f}_n] = \hat{\mathbf{A}}_n [\mathbf{c}] \tag{23}$$

where, [ ] represents the jump across the interface. Going through the procedure described by Roe (Roe 1981, LeVeque 1992), we find that if the following type of averaging is done, then the resulting linearized matrices preserve the jump conditions at the interface.

$$\hat{\mathbf{c}} = \frac{H_L^{-1/2}\mathbf{c}_L + H_R^{-1/2}\mathbf{c}_R}{H_L^{-1/2} + H_R^{-1/2}} \quad ; \quad \hat{\mathbf{A}} = \hat{\mathbf{A}}\left(\hat{\mathbf{c}}\right) \quad ; \quad \hat{\mathbf{B}} = \hat{\mathbf{B}}\left(\hat{\mathbf{c}}\right) \tag{24}$$

The Roe-linearized normal Jacobian matrix $\hat{\mathbf{A}}_n$ is found to be:

$$\hat{\mathbf{A}}_n = \begin{bmatrix} 0 & n_x & n_y \\ n_x\left(\hat{a}^2 - \hat{u}^2\right) - n_y \hat{u}\hat{v} & 2n_x\hat{u} + n_y\hat{v} & n_y\hat{u} \\ n_y\left(\hat{a}^2 - \hat{v}^2\right) - n_x \hat{u}\hat{v} & n_x\hat{v} & 2n_y\hat{v} + n_x\hat{u} \end{bmatrix} \tag{25}$$

where, $\hat{a}^2 = g\left(H_L + H_R\right)/2$. The Roe-linearized normal Jacobian matrix $(\hat{\mathbf{A}}_n)$ is same as the original nonlinear Jacobian matrix $(\mathbf{A}_n)$, except that the Roe-linearized velocities and fluid depth are used in place of the actual values. Thus, the eigenvalues and the eigenvectors have the same form as that given by Eqs.19-21, with the Roe-linearized variables used in place of the actual values.

Once the cell interface problem has been linearized, it is a simple matter to compute the normal flux $\hat{\mathbf{f}}_n$. It is well known from the theory of linear hyperbolic systems that an initial state that is discontinuous across an interface evolves in time in such a manner that the discontinuities propagate with the characteristic speeds given by the eigenvalues. The evolution of the cell interface problem in time is shown schematically in Fig.3. The following relations give the relation between the various states across the discontinuities:

$$\mathbf{c}_{m1} = \mathbf{c}_L + \alpha_1 \hat{\mathbf{r}}_1, \tag{26}$$

$$\mathbf{c}_{m2} = \mathbf{c}_{m1} + \alpha_2 \hat{\mathbf{r}}_2, \tag{27}$$

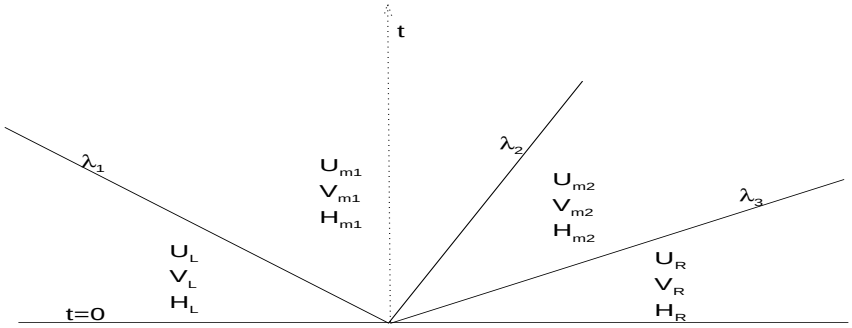

Figure 3: Evolution of the linearized cell interface problem

$$\mathbf{c}_R = \mathbf{c}_{m2} + \alpha_3 \hat{\mathbf{r}}_3. \tag{28}$$

Knowing $\mathbf{c}_L$ and $\mathbf{c}_R$, the weighting factors α_1, α_2 and α_3 can be computed. Knowing the weighting factors the Roe-Riemann flux at the interface is given by:

$$\hat{\mathbf{f}}_n\left(\mathbf{c}_L, \mathbf{c}_R\right) = \mathbf{f}_n\left(\mathbf{c}_L\right) + \sum_{p=1}^{p=3} \hat{\lambda}_p^- \alpha_p \hat{\mathbf{r}}_p \tag{29}$$

where, $\hat{\lambda}_p^- = min(\hat{\lambda}_p, 0)$. Once the numerical fluxes are computed, the state at the next time level is easily determined in an explicit fashion through Eq.15. Since this is a completely explicit procedure, the time step is limited by the CFL condition stated as:

$$\Delta t \leq inf \frac{h_e}{\lambda_{max}} \tag{30}$$

where, the infimum is taken over all numerical elements in the domain, h_e is a suitable measure of the size of the cell, and λ_{max} is the maximum eigenvalue for the cell.

The numerical algorithm as described above is first-order accurate in space and time, and is conservative and monotone.

4 RESULTS AND DISCUSSION

The Godunov-type finite volume method described in the previous section has been tested by simulating several benchmark and realistic coastal flow problems. The results obtained and their comparison to analytical and wave formulation based numerical results are described in this section.

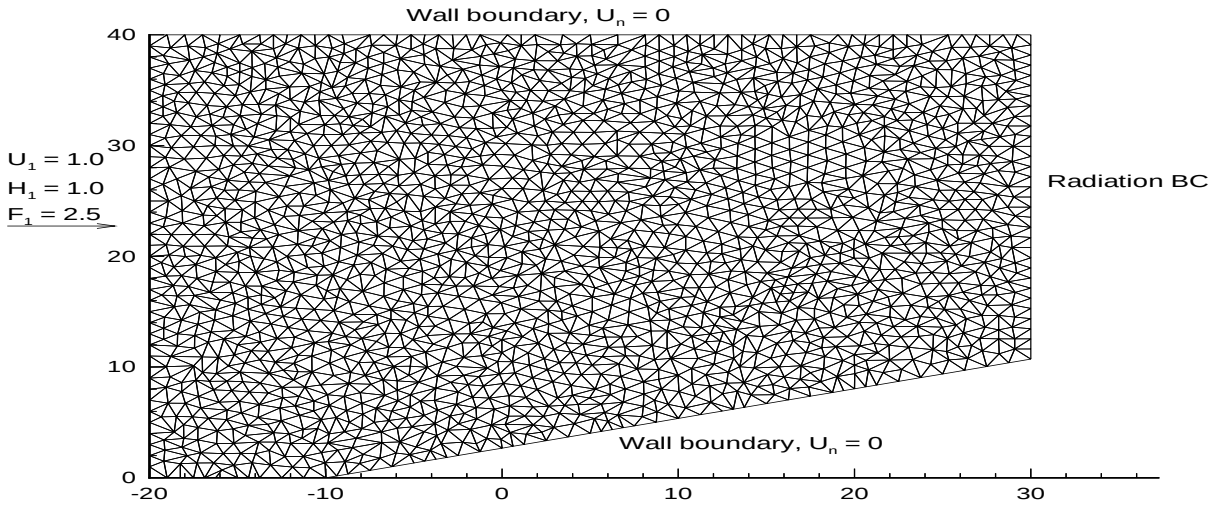

Figure 4: Numerical mesh and boundary conditions for supercritical flow past a channel constricted on one side.

4.1 SUPERCRITICAL CHANNEL FLOWS

Supercritical channel flows subject to a sudden change in cross-section can lead to the formation of hydraulic jumps (shocks) and negative jumps (rarefaction waves). Three different channel configurations have been used by Zienkiewicz and Ortiz (1995) to test their numerical scheme. We utilize these same channel configurations. For these channel flows, the inlet supercritical Froude number F_1 is defined as follows:

$$F_1 = \frac{U_1}{\sqrt{gH_1}}, \tag{31}$$

where U_1 and H_1 are the mean velocity and depth of the fluid at the inlet, respectively.

The first test case simulated is supercritical flow ($F_1 > 1$) encountering a sudden change of cross-section through a boundary wall constriction on one side wall of the channel. On the other side the flow remains unbounded. The channel geometry along with the numerical mesh and boundary conditions is shown in Fig.4. This type of channel geometry leads to the formation of a stationary hydraulic jump originating at the point of constriction. In all the supercritical cases simulated the channel has constant bathymetric depth, i.e., $\nabla h_b \equiv 0$. Numerical simulations were performed with a constriction angle of 15^0 and inlet supercritical Froude numbers $F_1 = 2.5$ and $F_1 = 3.0$. The numerical grid consists of 1957 nodes and 3734 triangular elements.

The steady state water depth for the two different inlet Froude numbers are shown in Figs.5 and 6. The results shown correspond to the basic Godunov method, i.e., piecewise constant approximation of all variables. The method is seen to be monotonic with no oscillations across the shock. The width of the shock

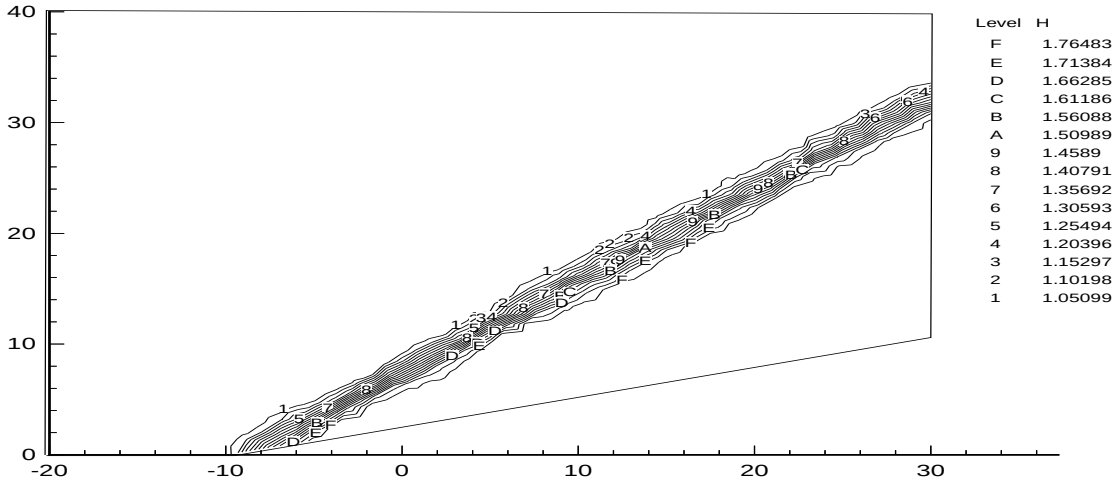

Figure 5: Contours of the fluid depth for $F_1 = 2.5$

F_1	θ_{num}	θ_{anal}
2.5	39.25	39.58
3.0	34.20	34.36

Table 1: Supercritical test case 1: comparison of the angle of the shock.

is seen to span only two to four cell divisions. Neglecting the viscous dissipation, this problem can be solved analytically (Ippen 1951). The angle of the shock predicted by the present numerical method is compared against the theoretical result in Table 4.1. Excellent agreement is seen.

In the second test case, the boundary wall is constricted on both sides, resulting in a cross-wave pattern. A constriction angle of $\beta = 5^0$ is applied on both sides of the channel and a supercritical flow with inlet Froude number $F_1 = 2.5$ is imposed (Fig.7). The numerical mesh consists of 1670 nodes and 3155 triangular elements. The steady state water depth is shown in Fig.8. Again, we observe very sharp resolution of the shock with monotonic behavior across the shock. Very good agreement with the theory is observed for the water depth in various regions of the channel (Table 4.1).

Region #	H_{num}	H_{anal}
1	1.00	1.00
2	1.25	1.254
3	1.527	1.55

Table 2: Supercritical test case 2: comparison of the the fluid depth in various regions of the flow.

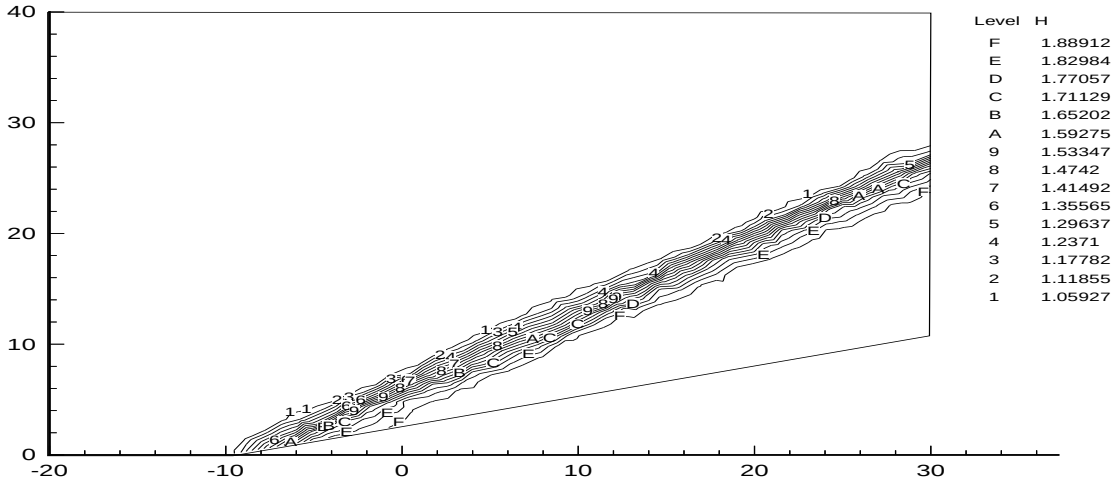

Figure 6: Contours of the fluid depth for $F_1 = 3.0$

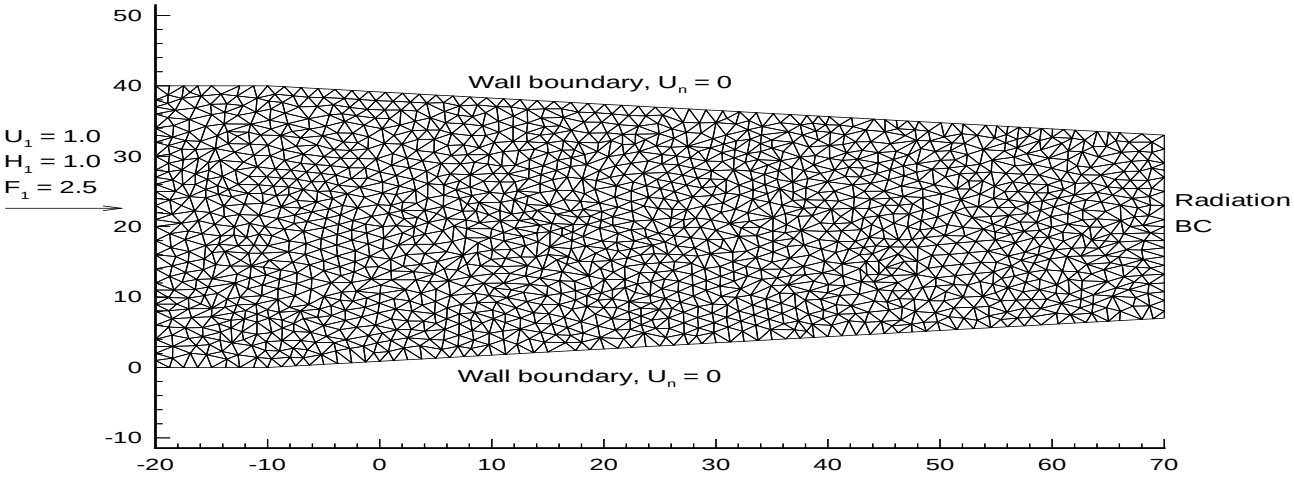

Figure 7: Numerical mesh and boundary conditions for supercritical flow past a channel constricted on both sides.

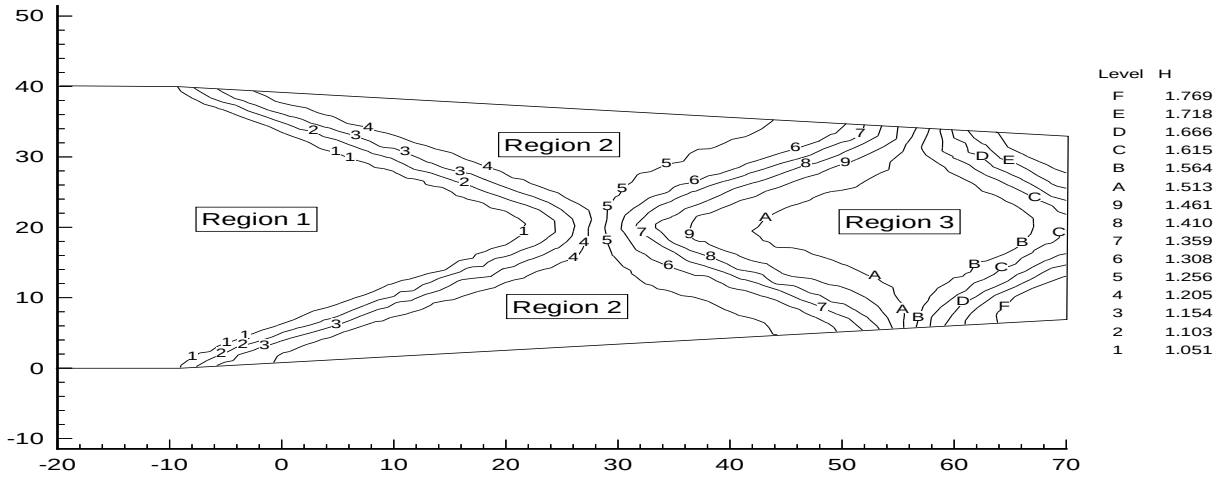

Figure 8: Contours of the fluid depth for $F_1 = 2.5$

Lastly, we consider a more complicated channel geometry (Fig.9). Due to the presence of concave corners, in this case we also have 'negative' waves, across which the fluid depth decreases, in addition to 'positive' jumps. The constriction angle is 15^0 followed downstream by enlargement. The inlet supercritical Froude number is $F_1 = 2.5$. The numerical mesh consists of 2342 nodes and 4451 triangular elements. The steady state water depth is shown in Fig.10. Again, we find a sharp resolution of the shock, and the numerical scheme also handles 'negative' jumps and shock interactions very well.

4.2 QUARTER ANNULAR TEST PROBLEM

In the previous section, it has been established that the present numerical scheme performs very well in the case of high Froude number flows, where there is a possibility of formation of hydraulic jumps and negative jumps. In this and subsequent subsections we consider real-life shallow water systems, which often have very complicated geomteries. The first problem considered is a quarter-annulus test problem (Lynch and Gray, 1978). The geometry and the finite element mesh are shown in Fig.11. The bathymetry varies quadratically from 10ft at the inner radius $r_1 = 2 \times 10^5$ft to 62.5ft at the outer radius $r_2 = 5 \times 10^5$ft. A tide with 12.4 hour period and 1ft amplitude is imposed along the sea boundary. The linear bottom friction parameter τ is set to $0.0001 s^{-1}$ and the Coriolis parameter is set to zero. The simulations are performed from a cold start with $\xi = 0$ and $u = v = 0$, and the open boundary forcing is gradually applied through a hyperbolic tangent ramp function over a period of four days. The simulation was run for 10.0 days and the elevation and velocities were measured at three stations with coordinates $(126697.0, 389933.0)$,

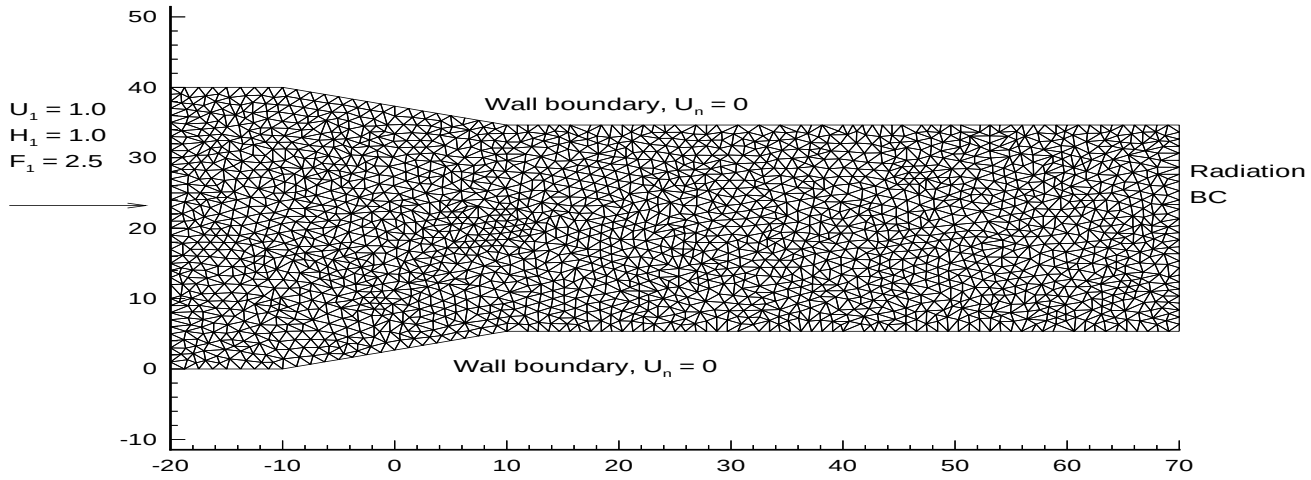

Figure 9: Numerical mesh and boundary conditions for supercritical flow past a channel having both constrictions and expansions.

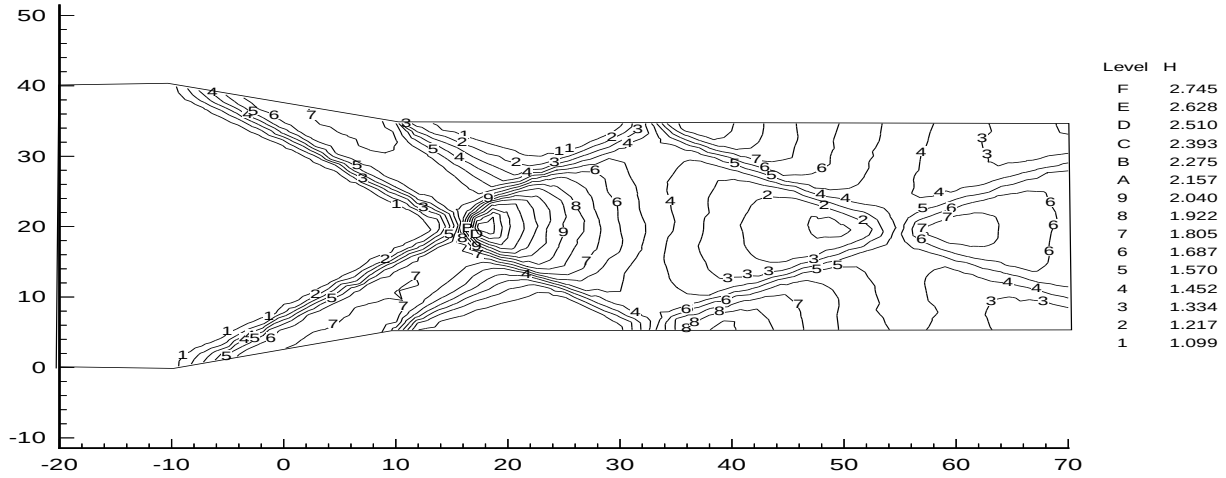

Figure 10: Contours of the fluid depth for $F_1 = 2.5$

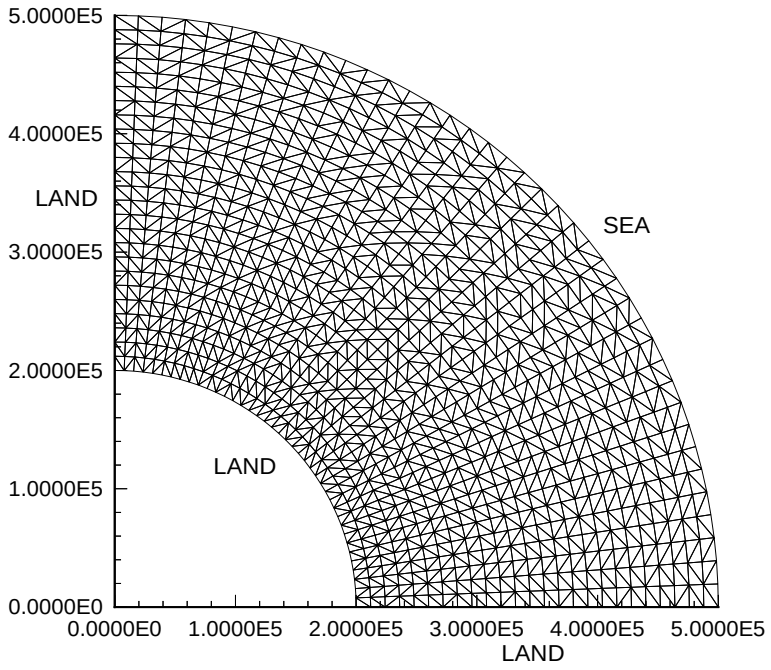

Figure 11: Numerical mesh and boundary conditions for the quarter annulus problem. Lengths are in ft.

(380238.0, 276259.0), and (218743.0, 71073.0) starting from the fifth day. The results obtained are compared with the predictions made by the ADCIRC (an advanced three-dimensional circulation model for shelves, coasts and estuaries) code which solves the SWE numerically through the use of Generalized Wave Continuity Equation (GWCE) formulation (Luettich et al. (1991)). The accuracy of this procedure has been established through comparisons with several test problems and field data and is used by many state and federal agencies.

We find excellent agreement between the present approach and ADCIRC as seen through Fig.12-14. The elevation and velocity field did not exhibit any spatial oscillations and the accuracy we get is of the same order as that obtained through the wave formulation.

4.3 TIDAL WAVES NEAR BAHAMAS ISLANDS

Tide-driven fluid flow near the Bahamas Islands is simulated next. The numerical mesh and physical geometry are shown in Fig.15. The bathymetry is shown in Fig.16. The following tidal forcing with time(t) in

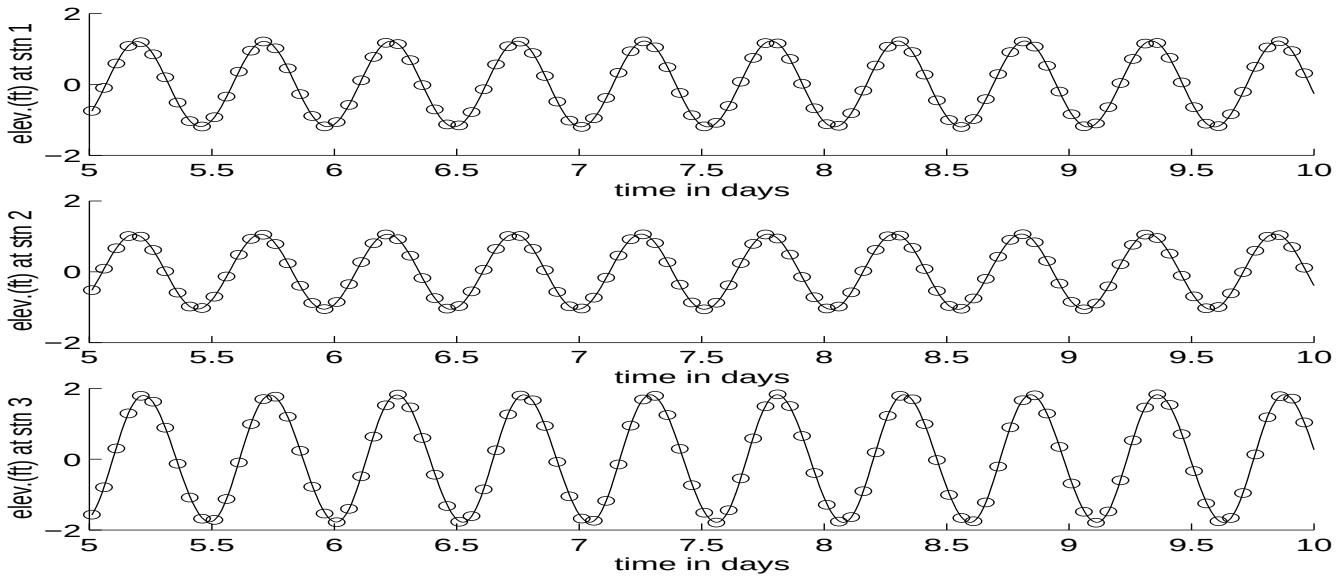

Figure 12: Station recordings of the elevation: present formulation(solid line) and ADCIRC(open circles).

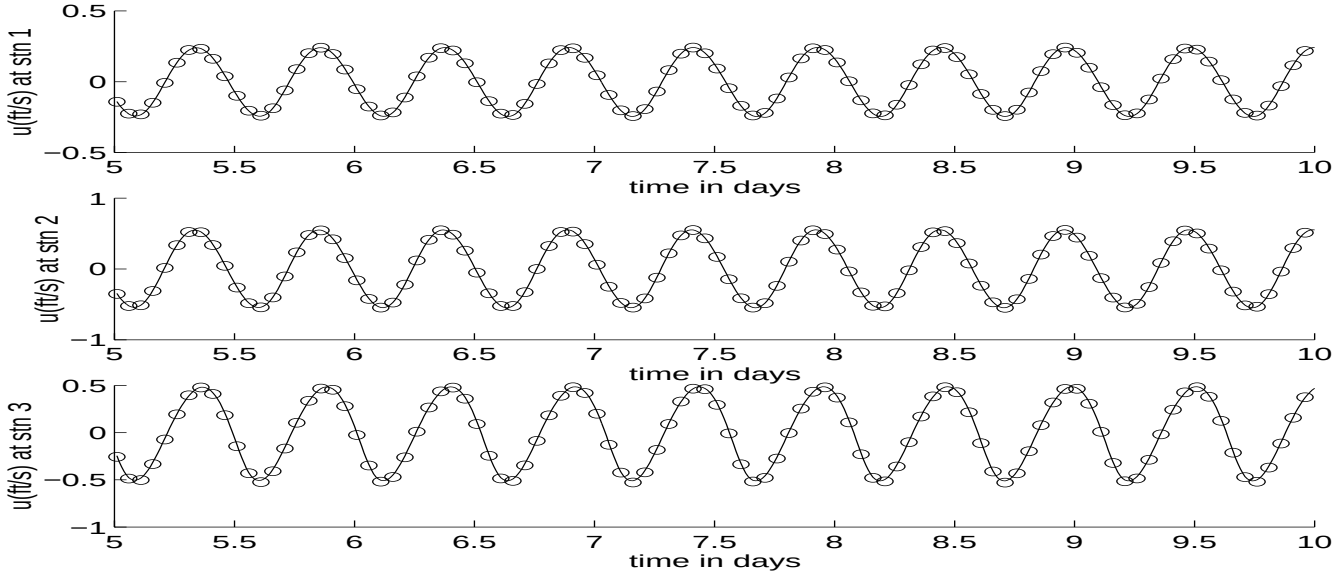

Figure 13: Recordings of the velocity in the x-direction at the three stations: solid line represents the present formulation and the open circles are the ADCIRC predictions.

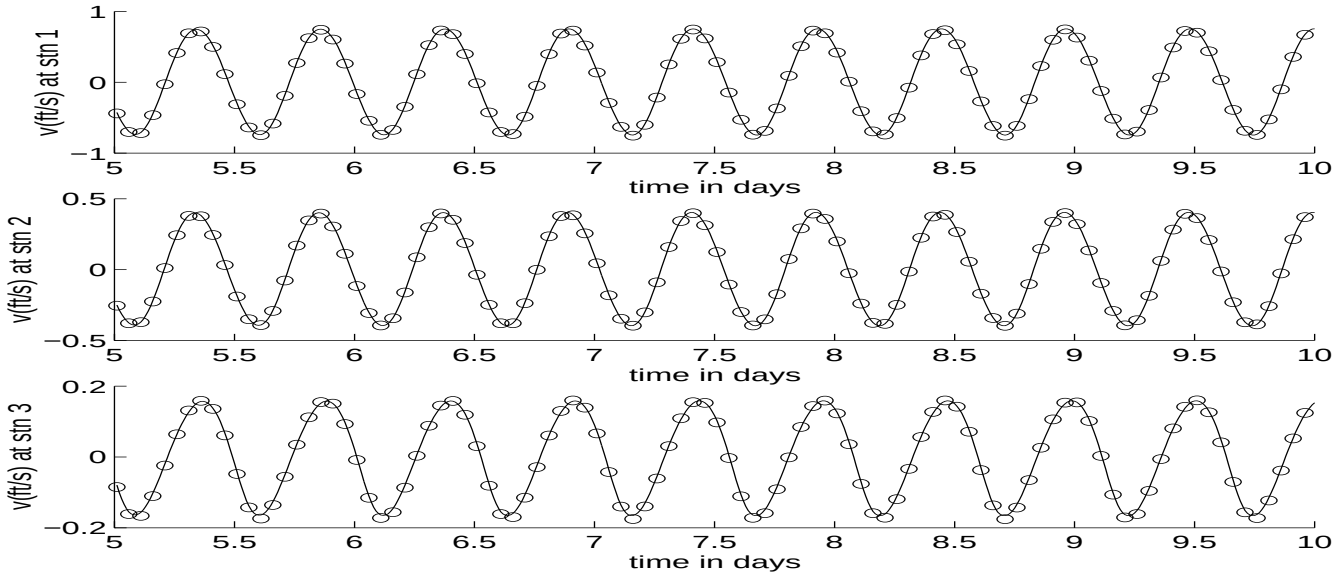

Figure 14: Recordings of the velocity in the y-direction at three stations: solid line represents the present formulation and the open circles are the ADCIRC predictions.

hours was imposed at the open sea boundary:

$$\begin{aligned}\hat{\xi}(t) &= 0.075\cos(\tfrac{t}{25.82}+3.40)\\ &+ 0.095\cos(\tfrac{t}{23.94}+3.60)\\ &+ 0.100\cos(\tfrac{t}{12.66}+5.93)\\ &+ 0.395\cos(\tfrac{t}{12.42}+0.00)\\ &+ 0.060\cos(\tfrac{t}{12.00}+0.75)\quad (meters).\end{aligned} \tag{32}$$

The bottom friction was imposed using the Chezy-friction law with friction coefficient 0.0001 and the Coriolois parameter was set to $3.19 \times 10^{-5} s^{-1}$. The simulations were cold started and the tidal forcing are imposed gradually through a ramp function over a period of two days. The elevation and velocities are measured at four different stations whose coordinates in meters are: $(38666.66, 49333.32)$, $(56097.79, 9612.94)$, $(41262.60, 29775.73)$, and $(59594.66, 41149.62)$. The results obtained are compared with the predictions made by ADCIRC and the elevation and x-velocity recordings at the four stations are shown in Fig.17-19. We obtain excellent agreement between both the methods, showing that the present numerical approach is atleast as accurate as the GWCE-NCME based finite element procedure.

The free surface deflection and the vector field of the total flow discharge $\mathbf{U} = \mathbf{u}H$ in steps of 1/4 days starting from the 11th day to the 12th day of the simulation are shown in Figs.20-24. In a high tide situation, i.e. the free surface is above the mean sea level, the fluid flow is into the domain, and vice versa in the case of a low tide situation. The approximate periodicity of the tide is around 12.4 hour, which is the most dominant tide applied at the open sea boundary. The flow patterns are complicated due to the presence of the islandand the geometrical shape of the physical domain. The tidal wave amplitude defined as the

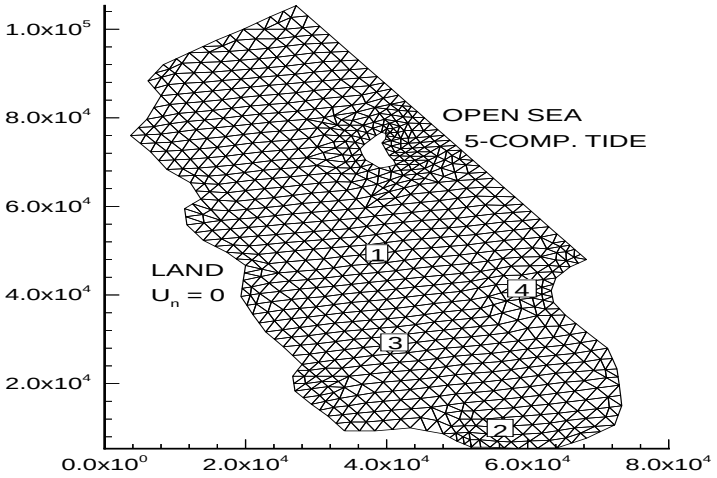

Figure 15: Numerical mesh and for tide-driven flow past an island. Lengths are in meters.

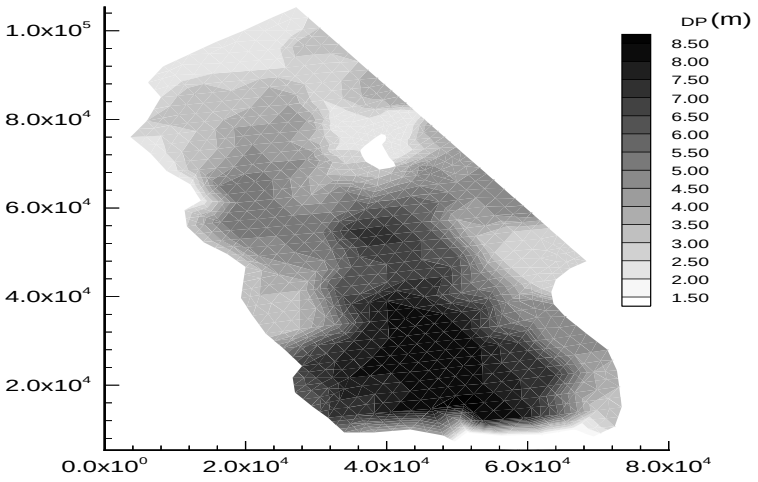

Figure 16: Bathymetry for tide-driven flow around an island. Lengths are in meters.

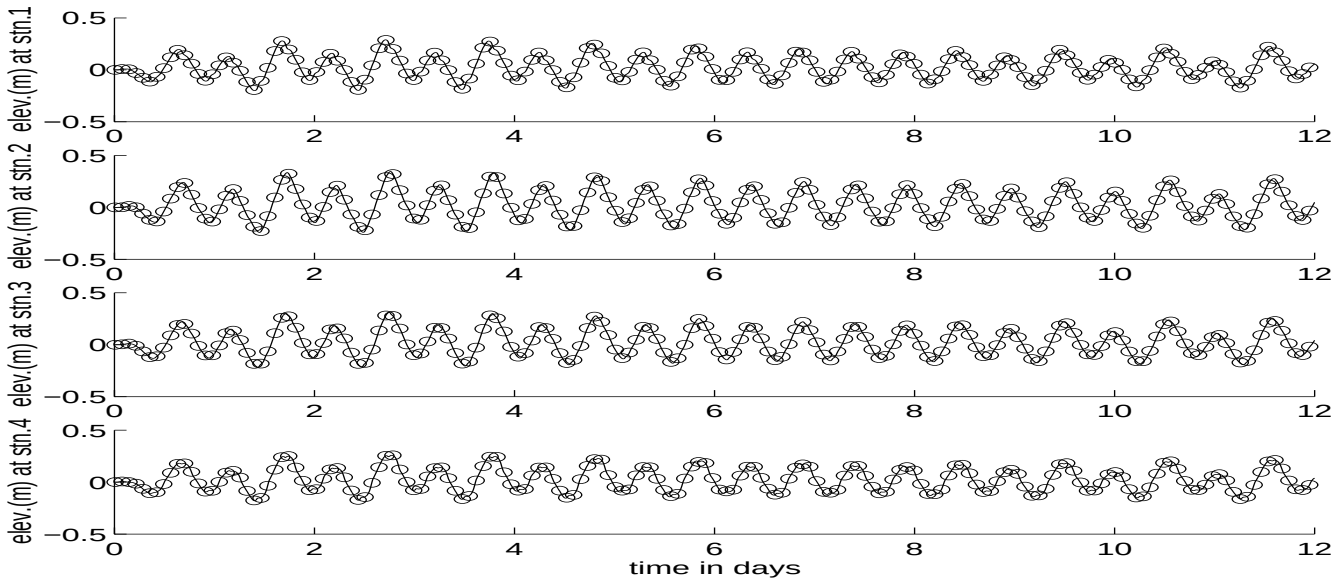

Figure 17: Elevation recordings at four stations: present formulation (soild line) and ADCIRC (open circles).

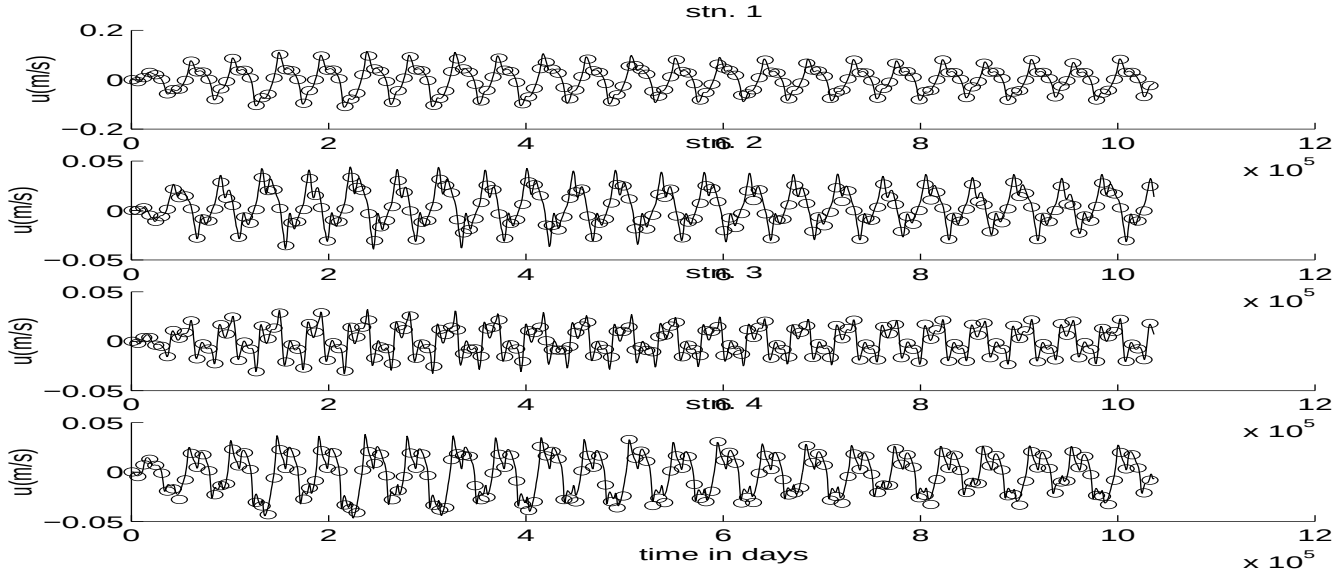

Figure 18: x-velocity recordings at four stations: present formulation (solid line) and ADCIRC (open circles).

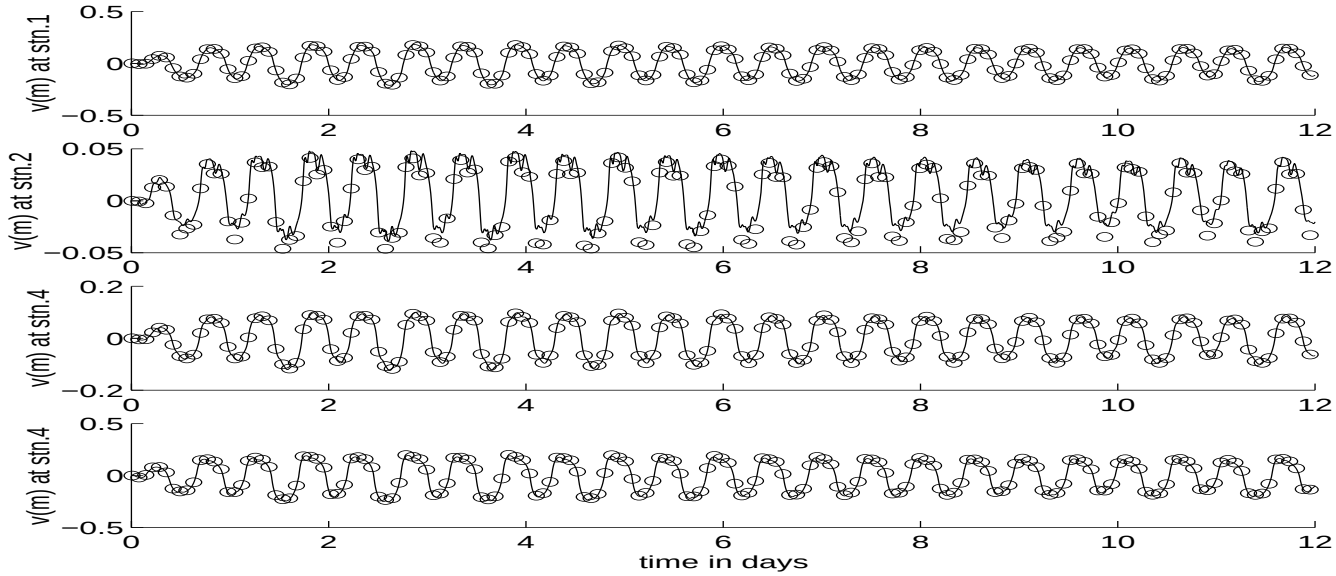

Figure 19: y-velocity recordings at four stations: present formulation (solid line) and ADCIRC (open circles).

difference between the maximum and minimum free surface heights is shown in Fig.25. We find that the tidal amplitude steadily decreases as we go inwards into the physical domain. The island breaks up the tidal wave front and the rear side of the island is shielded from the tidal wave.

4.4 TIDAL WAVES IN THE GALVESTON BAY

Tidal waves in the Galveston Bay are simulated next. The numerical and the bathymetry are shown in Figs.26 and 27. The physical domain is very complicated, with slender channel-like regions conneted to large lake-like water body. There are in total 17 islands in the physical domain. the bathymetry varies sharply near the Houston ship channel area. The boundary condition is the same as that applied in the previous simulation. A 5-component tidal forcing of the following form with time(t) in hours was imposed at the open sea boundary:

$$\begin{aligned} \hat{\xi}(t) &= 0.075\cos(\tfrac{t}{25.82}+3.40)+0.095\cos(\tfrac{t}{23.94}+3.60) \\ &+ 0.100\cos(\tfrac{t}{12.66}+5.93)+0.395\cos(\tfrac{t}{12.42}+0.00) \\ &+ 0.060\cos(\tfrac{t}{12.00}+0.75) \quad (meters). \end{aligned} \tag{33}$$

At the land and island boundaries we impose zero normal flux conditions. The bottom friction was imposed using the Chezy-friction law with friction coefficient 0.0040 and the Coriolois parameter was set to $7.07 \times 10^{-5} s^{-1}$. The simulations were cold started and the tidal forcings at the open sea boundary are imposed gradually through a ramp function over a period of two days. The simulations were run for a total of 12.0 days.

The time traces of the elevation and velocity field was recorded at 29 different stations spread out across

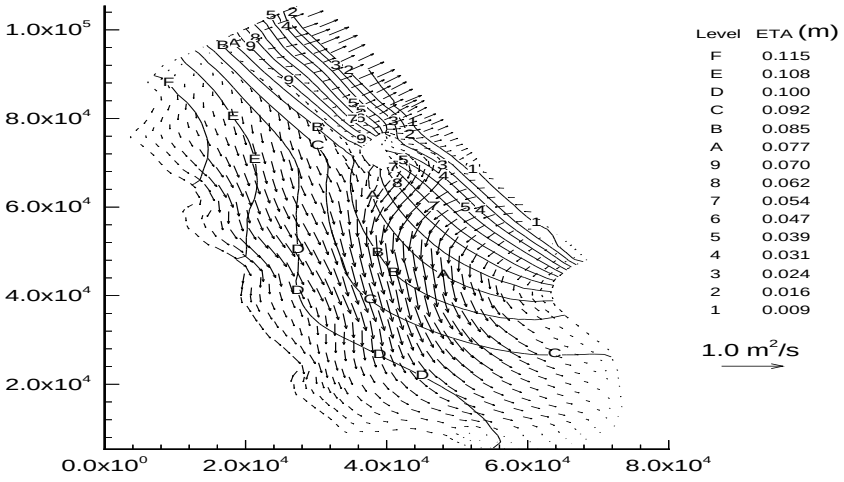

Figure 20: Free surface deflection (ξ) and flow field at $t = 11.00$ days. The vector field plotted is the discharge $\mathbf{U} = \mathbf{u}H$.

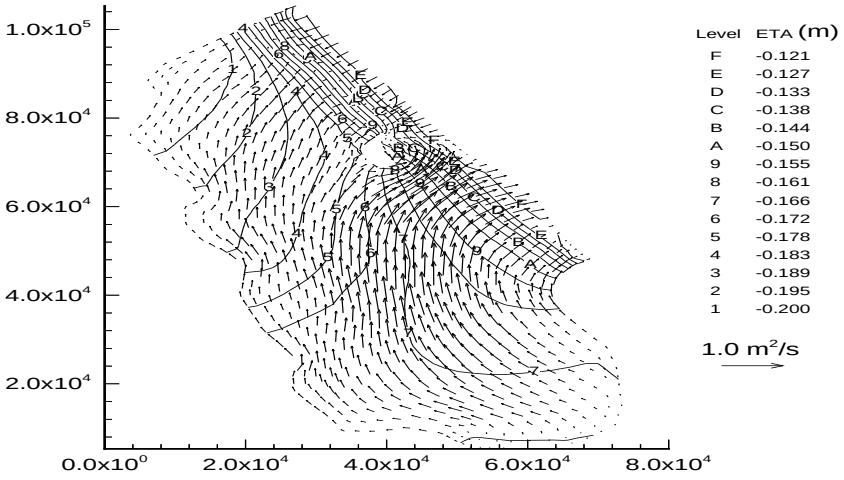

Figure 21: Free surface deflection (ξ) and flow field at $t = 11.25$ days. The vector field plotted is the discharge $\mathbf{U} = \mathbf{u}H$.

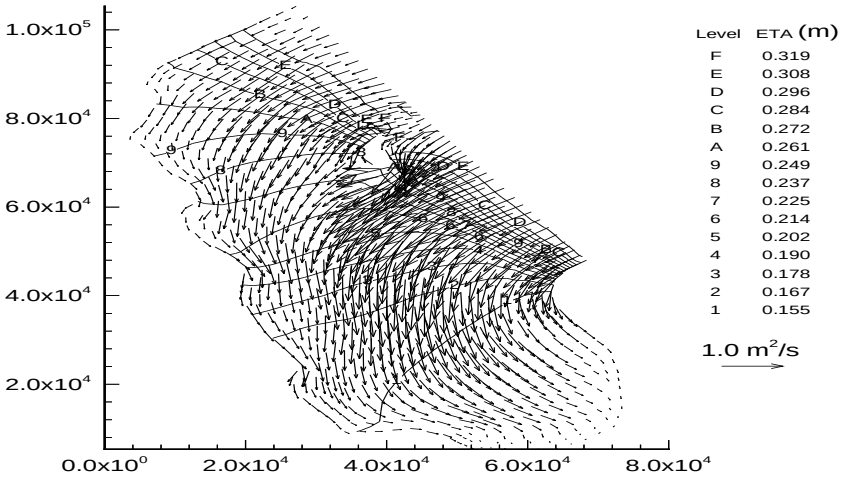

Figure 22: Free surface deflection (ξ) and flow field at $t = 11.50$ days. The vector field plotted is the discharge $\mathbf{U} = \mathbf{u}H$.

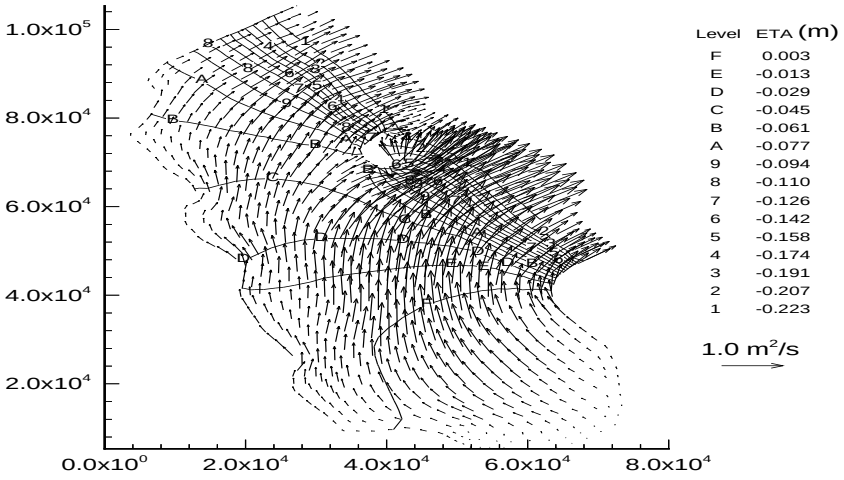

Figure 23: Free surface deflection (ξ) and flow field at $t = 11.75$ days. The vector field plotted is the discharge $\mathbf{U} = \mathbf{u}H$.

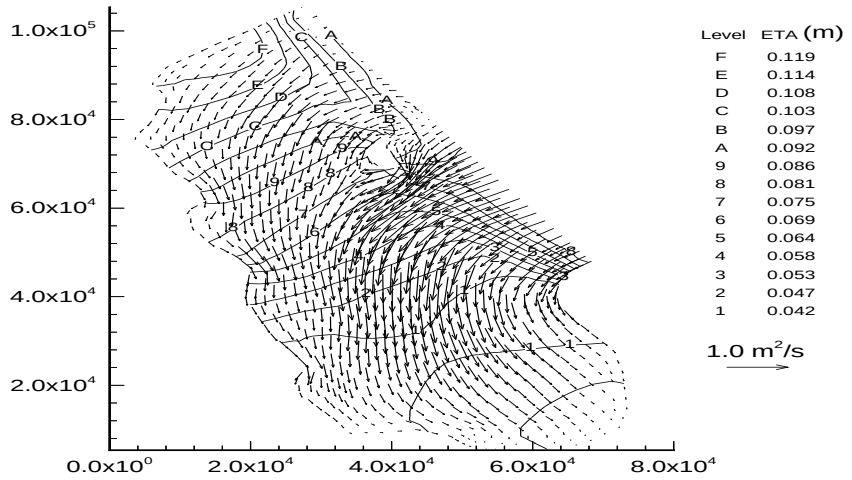

Figure 24: Free surface deflection (ξ) and flow field at $t = 12.00$ days. The vector field plotted is the discharge $\mathbf{U} = \mathbf{u}H$.

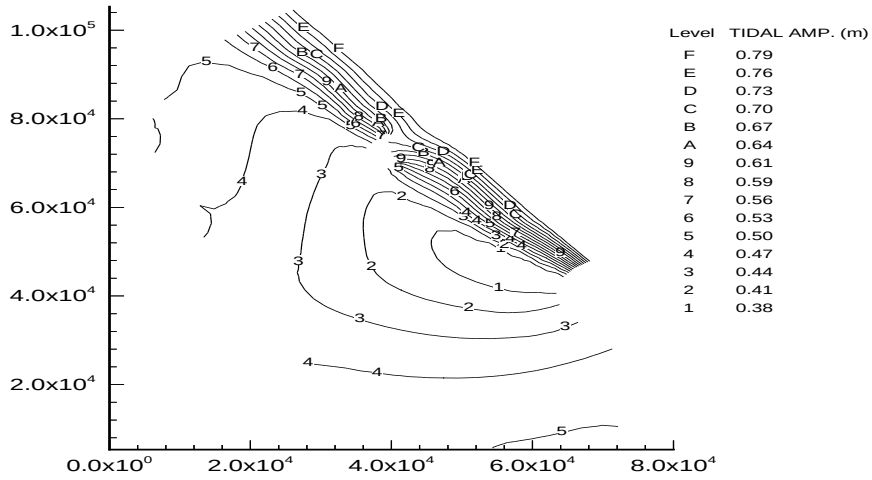

Figure 25: The tidal wave amplitude, $max(\xi) - min(\xi)$.

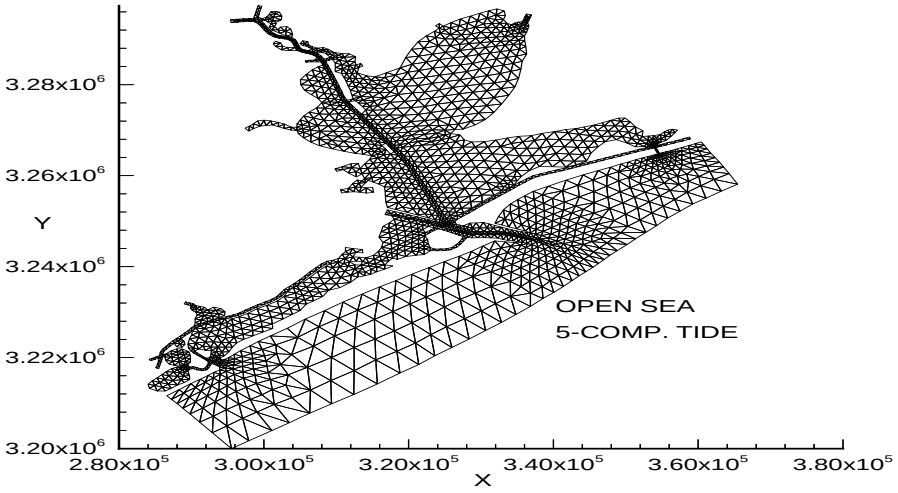

Figure 26: Galveston Bay: Numerical mesh.

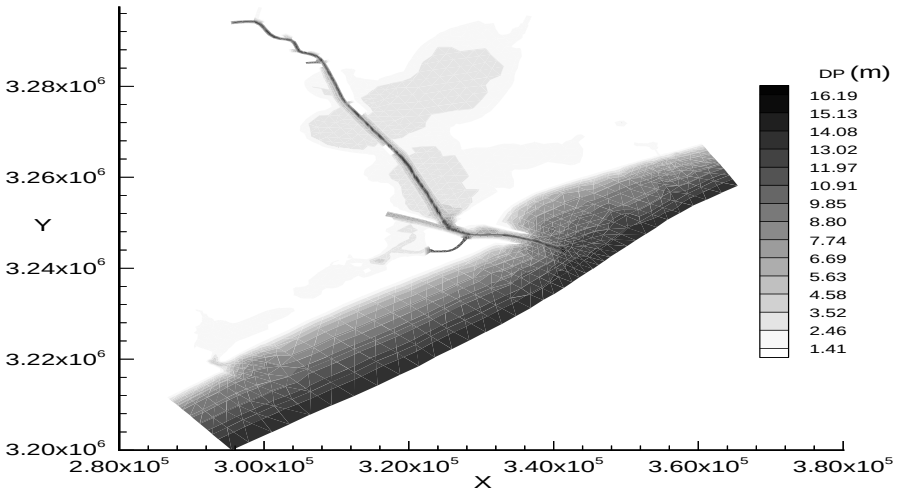

Figure 27: Galveston Bay: Bathymetry.

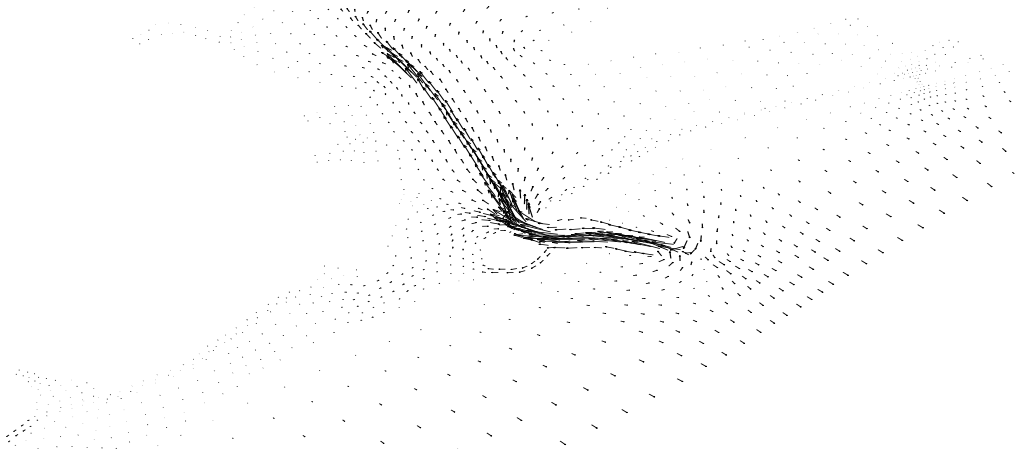

Figure 28: The flow discharge vector field ($\mathbf{U} = \mathbf{u}H$) at $t = 11.00$ days.

the physical domain. Good agreement with the predictions made by the ADCIRC code was observed at most of these stations.

The vector field of the total fluid discharge $\mathbf{U} = \mathbf{u}H$ in intervals of 1/4 days from the 11th day to the 12th day are shown in Figs.28-32. The Galveston Island and the Bolivar Peninsula (the two long slender islands) shield the interior of the Bay from the tidal waves. We find that tidal flow enters and leaves the Bay primarily through the Houston Shipping Channel. In Fig.33 the tidal wave amplitude defined as the difference between the wave peak and the wave trough is shown. The islands shield the region behind them from the tidal fluctuations.

5 HIGHER-ORDER EXTENSION

In §3, the basic Godunov-based finite volume scheme has been described. In §4, the method has been tested on some simple test problems as well as complex coastal flow problems, and was shown to be robust and monotone without producing any spurious spatial oscillations. The method as described in §3 is however, only first-order accurate in space. In this section, we discuss the extension of the basic Godunov-type finite volume method described in §3 to higher-order spatial accuracy.

First-order upwind methods are monotone and resolve discontinuities without producing any oscillations. However, in smooth portions of the flow, the first-order accuracy is not sufficient. Second-order methods based on central-difference type approximations give good accuracy in smooth portions of the flow, but produce oscillations in the vicinity of discontinuities, and thus are not monotone. Several high resolution

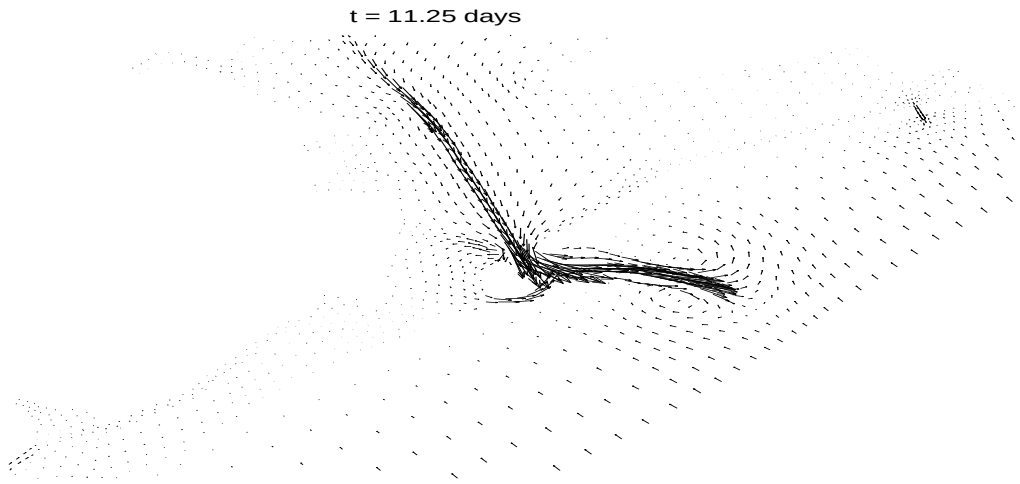

Figure 29: The flow discharge vector field ($\mathbf{U} = \mathbf{u}H$) at $t = 11.25$ days.

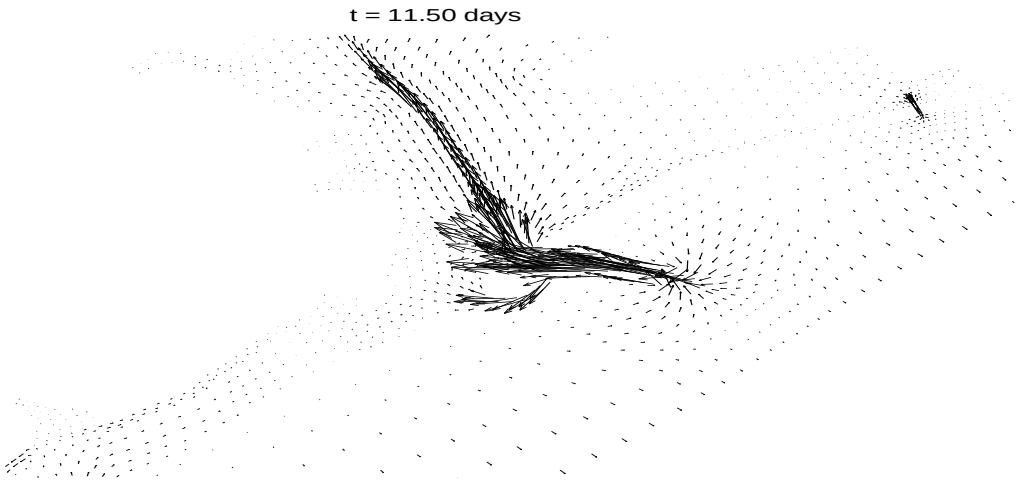

Figure 30: The flow discharge vector field ($\mathbf{U} = \mathbf{u}H$) at $t = 11.50$ days.

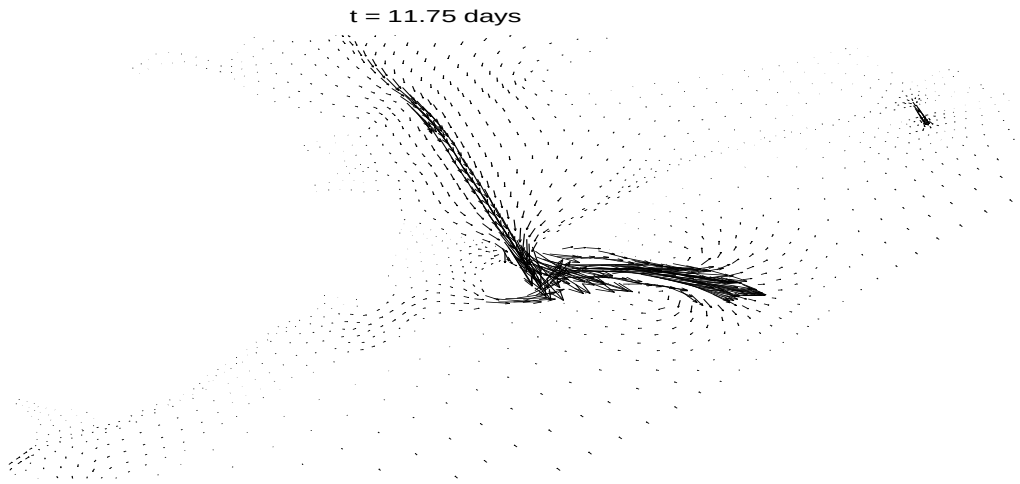

Figure 31: The flow discharge vector field ($\mathbf{U} = \mathbf{u}H$) at $t = 11.75$ days.

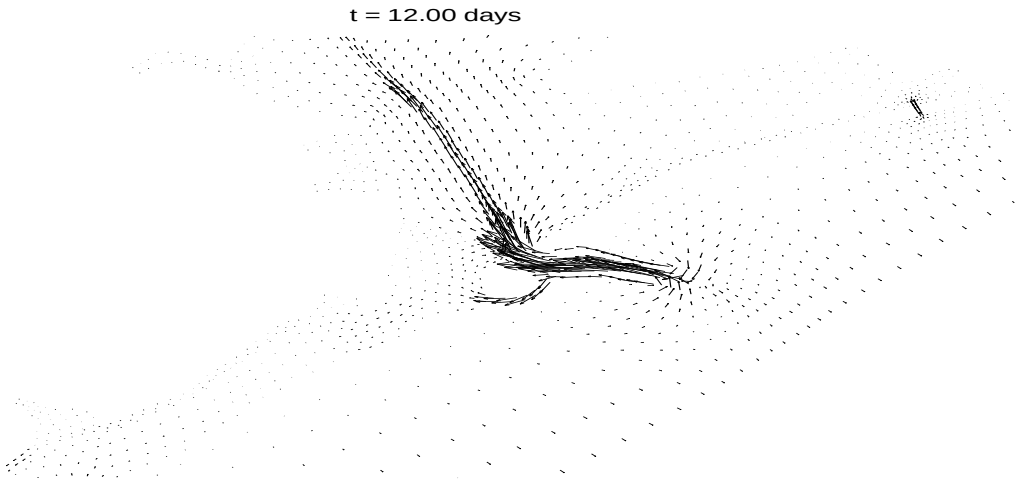

Figure 32: The flow discharge vector field ($\mathbf{U} = \mathbf{u}H$) at $t = 12.00$ days.

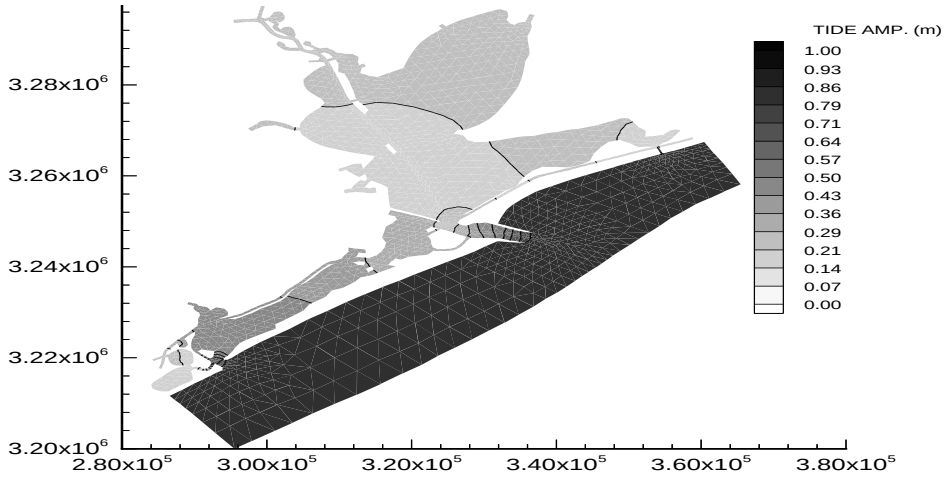

Figure 33: Tidal wave amplitude (max(ξ) - min(ξ)).

methods have been constructed that give higher-order accuracy in smooth portions of the flow but reduce to a first-order method near discontinuities. In this manner, higher-order (that is better than first-order) monotone methods can be constructed. These higher-order monotone methods are usually of the flux-limiter type (Boris and Book (1973), Van Leer(1974), Zalesak(1979), Harten (1983), Osher and Chakravarthy (1984)) or the slope-limiter type (Colella and Woodward (1984), Harten, Engquist, Osher and Chakravarthy (1987), Harten and Osher (1987), Van Leer (1977a, 1977b, 1979), Colella (1985), Goodman and Le Veque (1988), Harten (1987), Harten, Engqusit, Osher and Chakravarthy (1987), Harten, Osher, Engquist and Chakravarthy (1986), Shu and Osher (1988), Shu and Osher (1989), Bell, Dawson and Shubin (1988)).

We extend the basic Godunov-based finite volume numerical scheme to second order spatial accuracy using slope limiters. From the piecewise constant cell-averages, we construct piecewise linear representation for each primary variables ξ, U, V. Thus, within each triangular element the primary variables are linear but could be discontinuous across the element edges. We first describe the slope reconstruction method for a scalar conservation equation. We then extend this procedure to the system of SWE.

The slope computation can be thought to consist of two steps, namely, the reconstruction step, and the limiting step. In the reconstruction step, we compute slopes for each of the scalar variable c knowing its cell averages in the following manner. Within each cell, c is expressed as a piecewise linear function of the following form:

$$c_i^R = \bar{c}_i + \left(\frac{\partial c}{\partial x}\right)_i (x - \bar{x}_i) + \left(\frac{\partial c}{\partial y}\right)_i (y - \bar{y}_i) \tag{34}$$

The c_i^R is the reconstructed field, $\bar{c}_i$ is the cell-average, and $(\bar{x}_i, \bar{y}_i)$ is the centroid of the cell. The subscript

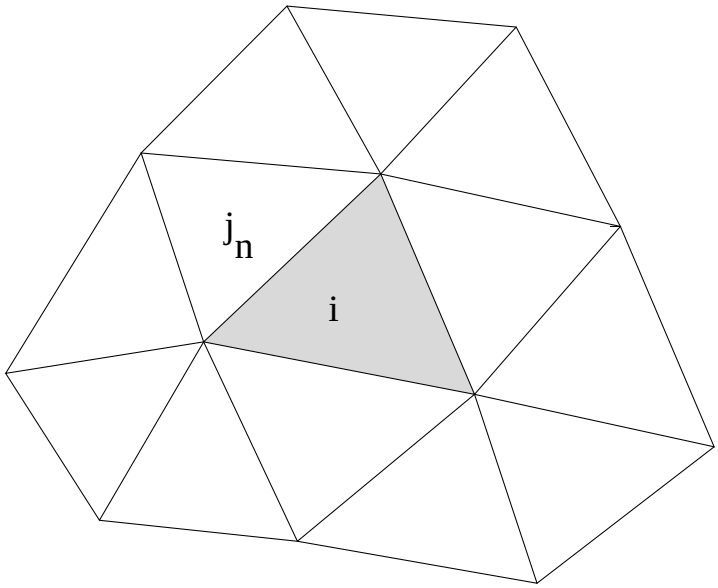

Figure 34: The patch used for computing slopes

i denotes the cell number, and the superscript R stands for the reconstructed field. The piecewise constant field is constructed in such a way that when averaged over the cell we get back the original cell-average, and in this way we maintain the conservative property of the overall numerical scheme. The slopes are computed using the cell-averages in the neighboring cells (Fig.34). The following constraints are imposed on the reconstructed field:

$$\int_{A_{j_n}} c_i^R \, dA_{j_n} = \bar{c}_{j_n} A_{j_n}, \quad n = 1, \ldots, N \tag{35}$$

where j_n are neighbouring elements (Fig.34) and N is the total number of neighboring elements of element i. Since typically we have more constraints than unknowns, the slopes are computed through least-squares minimization.

The slopes obtained in the above manner do not in general satisfy the total variation bounded (TVB) property, and some type of limiting needs to be applied. In a linear triangle the extrema occur at the vertices. Hence the slopes are adjusted so that no new extrema are created in the field by iterating over the vertices. The reconstruction step and the limiting step together result in a linear slope reconstruction procedure that is both conservative and total variation bounded (TVB).

A straight forward extension of the above procedure to each of the primary variables in the case of a system of conservation laws might not always work. We did extensive testing in the context of shallow water equations with this type of approach, but found it to be unstable in certain situations, especially when there are large bathymetric gradients and sharp corners. We developed a new slope reconstruction procedure for the system of conservation laws based on local linearzation and reformulating the equations so that they get

decoupled. This procedure in the context of SWE is briefly described below.

The SWE given by Eq.11 are linearized for the element we wish to reconstruct the slopes in the following manner:

$$\frac{\partial \mathbf{c}}{\partial t} + \mathbf{A}_n \frac{\partial \mathbf{c}}{\partial n} = 0 \tag{36}$$

The normal jacobian matrix $\mathbf{A}_n$ is given by Eq.18. This element-level linear system can be decoupled using the eigen matrix given by:

$$\mathbf{R} = \begin{bmatrix} 1 & 0 & 1 \\ u - \sqrt{gH} n_x & -n_y & u + \sqrt{gH} n_x \\ v - \sqrt{gH} n_y & n_x & v + \sqrt{gH} n_y \end{bmatrix} \tag{37}$$

Defining a new set of variables $\mathbf{d}$ as:

$$\mathbf{d} = \mathbf{R}^{-1} \mathbf{c} \tag{38}$$

the linearized SWE given by Eq.36 can be written as a decoupled system given by:

$$\frac{\partial \mathbf{d}}{\partial t} + \Lambda \frac{\partial \mathbf{d}}{\partial n} = 0 \tag{39}$$

where $\Lambda = \mathbf{R} \mathbf{A}_n \mathbf{R}^{-1}$ is a diagonal matrix consisting of the eigenvalues of the jacobian $\mathbf{A}_n$. The slopes are computed for each of the individual component of $\mathbf{d}$ separately and are converted into slopes of $\mathbf{c}$ using the following relationship:

$$\frac{\partial \mathbf{c}}{\partial x} = \mathbf{R} \frac{\partial \mathbf{d}}{\partial x}; \quad \frac{\partial \mathbf{c}}{\partial y} = \mathbf{R} \frac{\partial \mathbf{d}}{\partial y}. \tag{40}$$

It turns out that for the SWE, $\mathbf{d}$ has a very simple form given by:

$$\mathbf{d} = \begin{Bmatrix} H/2 \\ 0 \\ H/2 \end{Bmatrix}. \tag{41}$$

Thus, it is enough to calculate the slope of the fluid depth $H = \xi + h_b$, and using this the slopes for the remaining primary variables U, V can be found using Eq.40. The slopes for U and V are given by:

$$\frac{\partial U}{\partial x} = u \frac{\partial H}{\partial x}; \quad \frac{\partial U}{\partial y} = u \frac{\partial H}{\partial y}; \quad \frac{\partial V}{\partial x} = v \frac{\partial H}{\partial x}; \quad \frac{\partial V}{\partial y} = v \frac{\partial H}{\partial y}. \tag{42}$$

The above described procedure for computing the slopes for the primary variables H, U, V described by the SWE has some noteworthy physical characteristics. Before the slope reconstruction step what we have are piecewise constants for H, U, and V and also for the fluid velocities $u = U/h$ and $v = V/H$. Thus we have zero vorticity $\omega = \nabla \times \mathbf{u}$ within each cell. Even after the reconstruction step, we still preserve this cell-wise zero vorticity property. The other important property is that the reconstructed velocity field is divergence-free over each cell, i.e $\nabla \cdot \mathbf{u} \equiv 0$. The slope reconstruction is done at a fixed time level, i.e., the fluid mass over which the slope reconstruction is being done remains the same before and after the reconstruction. Hence the Lagrangian time derivative $(\frac{D}{Dt})$ of the mass and momemtum should not change

during the course of the slope reconstruction and this is ensured by the zero divergence condition enforced cell-by-cell. This should be apparent from rewriting the mass conservation equation in the following way:

$$\underbrace{\frac{\partial H}{\partial t} + \mathbf{u} \cdot \nabla H}_{\frac{DH}{Dt}} + H \nabla \cdot \mathbf{u} = 0 \tag{43}$$

The slope reconstruction procedure as described above results in a Godunov-type finite volume procedure that is spatially second-order accurate in smooth portions of the flow, and first order accurate near discontinuities. To make the scheme truly second-order, the temporal accuracy needs to be increased as well and this is done using the two step Runge-Kutta procedure proposed by Shu and Osher (1989). Let $L(\mathbf{c})$ represent the linear operator consisting of the higher-order fluxes obtained after slope reconstruction and the body forces. The SWE system can then be represented as:

$$\frac{\partial \mathbf{c}}{\partial t} = L\left(\mathbf{c}\right). \tag{44}$$

The two step Runge-Kutta procedure can then be written as:

Predictor step:

$$\hat{\mathbf{c}}^{n+1} = \mathbf{c}^n + \Delta t L\left(\mathbf{c}^n\right) \tag{45}$$

Corrector step:

$$\mathbf{c}^{n+1} = \mathbf{c}^n + \frac{\Delta t}{2}\left[L\left(\hat{\mathbf{c}}^{n+1}\right) + L\left(\mathbf{c}^n\right)\right] \tag{46}$$

The above described slope reconstruction procedure has been implemented on a variety of supercritical channel flows and real-life coastal flow problems. In all cases a stable monotone behavior was observed. The higher-order method has less artificial diffusion and the resolution of discontinuities is much sharper compared to the basic first-order method described in §5. The fluid depth contours obtained using the higher order method for supercritical channel configuration given by Fig.7 is shown in Fig.35. Compared to Fig.8 where the fluid depth contours obtained using the basic first-order Godunov method are shown, we find that the discontinuities are resolved much more sharply using the higher-order extension.

6 CONCLUSIONS AND FUTURE WORK

A numerical procedure based on the primitive form of the shallow water equations has been developed. This numerical procedure is shown to be stable and monotonic without leading to any spurious spatial oscillations. In addition, this procedure conserves mass and momentum locally. The present formulation has been compared to the wave formulation of Luettich et al.(1991), and very good agreement is found between both the approaches.

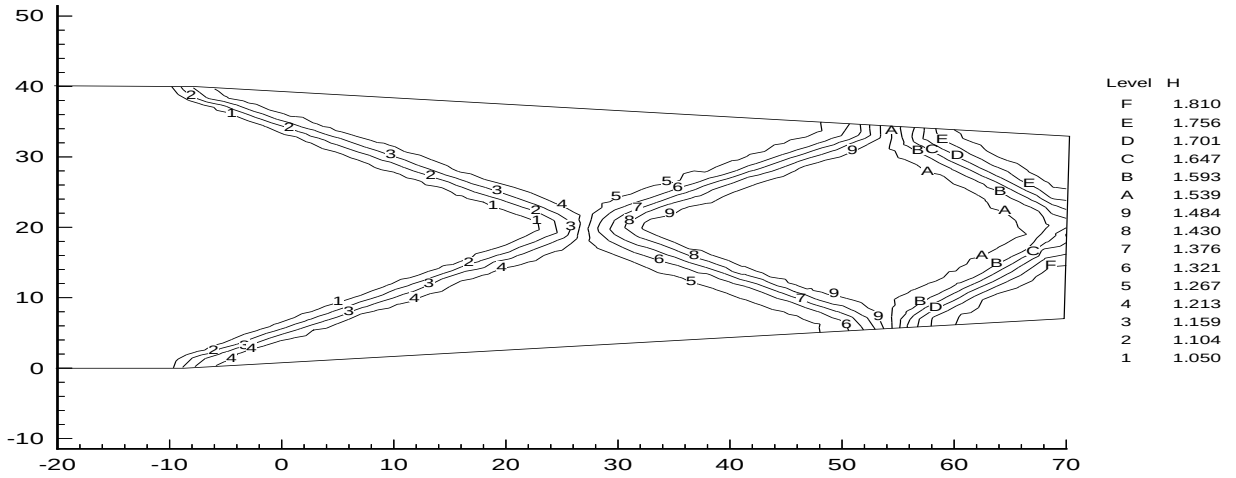

Figure 35: Contours of the fluid depth for $F_1 = 2.5$ using the higher-order Godunov method based on slope-limiter type algorithm.

There are several aspects of this problem that can be improved further. At present the scheme is limited by the CFL condition, and implicit temporal schemes that allow us to take larger time steps are worth looking into. From the modeling point of view, inclusion of the dissipation terms is necessary. In most physical situations, the bottom friction terms dominate the lateral diffusion and dispersion. However, there exist situations, especially those involving heavy mixing, where, the lateral diffusion and dispersion terms are important. Also important is the development of scalable parallel algorithms for parallel and distributed computing systems. The above listed areas are some of the avenues we are currently working on.

7 ACKNOWLEDGEMENTS

This work was partially funded by the National Science Foundation, Project No. DMS-9408151. The authors thank J.J.Westerink and W.G.Gray for sharing the ADCIRC code and data sets.

References

[1] Alcrudo, F., and Garcia-Navarro, P., 1993, "A high-resolution Godunov-type scheme in finite volumes for the 2D shallow-water equations," *Int. J. Num. Meth. Fluids*, **16**, pp.489-505.

[2] Bell, J. B., Dawson, C. N., and Shubin, G. R., 1988, "An unsplit, higher-order Godunov method for scalar conservation laws in two dimensions," *J. Comput. Phys.*, **74**, pp.1-24.

[3] Boris, J. P., and Book, D. L., 1973, "Flux corrected transport, I, SHASTA, A fluid transport algorithm that works," *J. Comput. Phys.*, **11**, pp.38-69.

[4] Colella, P., and Woodward, P. R., 1984, "The piecewise parabolic method (PPM) for gas dynamical calculations," *J. Comput. Phys.*, **54**, pp.174-201.

[5] Colella, P., 1985, "A direct Eulerian MUSCL scheme for gas dynamics," *SIAM J. Sci. Stat. Comput.*, **6**, pp.104-177.

[6] Godunov, S. K., 1959, "A difference scheme for numerical computation of discontinuous solution of hydrodynamics equations," *Math. Sbornik*, **47**, pp.271-306 (in Russian). Translated US Joint Publ. Res. Service, JPRS 7226 (1969).

[7] Goodman, J. B., and LeVeque, R. J., 1988, "A geometric approach to high resolution TVD schemes," *SIAM J. Num. Anal.*, **25**, pp.268-284.

[8] Harten, A., 1983, "High resolution schemes for hyperbolic conservation laws," *J. Comput. Phys.*, **49**, pp.357-393.

[9] Harten, A., Engquist, B., Osher, S. J., and Chakravarthy, S. R., 1986, "Some results on uniformly high-order accurate essentially nonoscillatory schemes," *J. Appl. Numer. Math.*, **2**, pp.347-377.

[10] Harten, A., 1987, "ENO schemes with subcell resolution," *J. Comput. Phys.*, **83**, pp.148-184.

[11] Harten, A., Engquist, B., Osher, S. J., and Chakravarthy, S. R., 1987, "Uniformly high order accurate essentially non-oscillatory schemes, III," *J. Comput. Phys.*, **71**, pp.231.

[12] Hirsch, C., 1990, *Numerical Computation of Internal and External Flows*, vol.2, John Wiley & Sons.

[13] Ippen, A. T., 1951, "Mechanics of supercritical flow," *Trans. ASCE*, **116**, pp.268-295.

[14] Kawahara, M., Hirano, H., Tsuhora, K., and Iwagaki, K., 1982, "Selective lumping finite element method for shallow water equations," Int. J. Num. Meth. Engg., **2**, pp.99-112.

[15] King, I.P., and Norton, W.R., 1978, "Recent application of RMA's finite element models for two-dimensional hydrodynamics and water quality," in Finite Elements in Water Resources II, C.A. Brebbia, W.G.Gray, and G.F.Pinder, eds., Pentech Press, London.

[16] Kinnmark, I., 1985, "The shallow water wave equations: formulation, analysis and application," Lecture Notes in Engineering, C. A. Brebbia and S. A. Orszag, ed., Springer-Verlag.

[17] LeVeque, R. J., 1992, *Numerical Methods for Conservation Laws*, Birkhauser Verlag.

[18] Luettich, Jr., R. A., Westerink, J. J., and Scheffner, N. W., 1991, "ADCIRC: An Advanced Three-Dimensional Circulation Model for Shelves, Coasts and Estuaries," Report 1, U.S. Army Corps of Engineers, Washington, D.C. 20314-1000, December 1991.

[19] Lynch, D.R., and Gray, W.G., 1978, "Analytic solution for computer flow model testing," ASCE J. Hydraulic Div., **104**, pp.1409-1428.

[20] Lynch, D.R., and Gray, W., 1979, "A wave equation model for finite element tidal computations," Comput. Fluids, **7**, pp.207-228.

[21] Navon, I.M., 1988, "A review of finite element methods for solving the shallow water equations," in B.Schreffler and O.C.Zienkiewicz, ed., Computer Modelling in Ocean Engineering, Balkeman, Rotterdam, pp.273-278.

[22] Osher, S., and Chakravarthy, S. R., 1984, "High resolution schemes and the entropy condition," *SIAM J. Num. Anal.*, **21**, pp.955-984.

[23] Roe, P. L., 1981, "Approximate Riemann solvers, parameter vectors, and difference schemes," *J. Comput. Phys.*, **43**, pp.357-372.

[24] Shu, C. -W., and Osher, S. J., 1988, "Efficient implementation of essentially nonoscillatory shock-capturing schemes," *J. Comput. Phys.*, **77**, pp.439-471.

[25] Shu, C. -W., and Osher, S. J., 1989, "Efficient implementation of essentially nonoscillatory shock-capturing schemes, II," *J. Comput. Phys.*, **83**, pp.32.

[26] Szymkiewicz, R., 1993, "Oscillation-free solution of shallow water equations for nonstaggered grid," J. Hyd. Engg., **119**, No.10, pp.1118-1137.

[27] Van Leer, B., 1974, "Towards the ultimate conservative difference schemes, II. Monotonicity and conservation combined in a second order scheme," *J. Comput. Phys.*, **14**, pp.361.

[28] Van Leer, B., 1977, "Towards the ultimate conservative difference scheme, III. Upstream-centered finite-difference schemes for ideal compressible flow," *J. Comput. Phys.*, **23**, pp.263.

[29] Van Leer, B., 1977, "Towards the ultimate conservative difference scheme, IV. A new approach to numerical convection," *J. Comput. Phys.*, **23**, pp.276.

[30] Van Leer, B., 1979, "Towards the ultimate conservative difference scheme, V. A second-order sequel to Godunov's method," *J. Comput. Phys.*, **32**, pp.101-136.

[31] Zalesak, S. T., 1979, "Fully multidimensional flux corrected transport algorithms for fluis," *J. Comput. Phys.*, **31**, pp.335-362.

[32] Zienkiewicz, O.C., and Ortiz, P., 1995, "A split-characteristic based finite element model for the shallow water equations," Int. J. Num. Meth. Fluids, **20**, pp.1061-1080.